Modelling the influence of microstructure on elastic properties and tensile damage behaviour of Mo-base silicide alloys

Dissertation

zur Erlangung des akadamischen Grades

Doktoringenieur
(Dr.-Ing.)

von: Praveen Goud Biragoni

geb. am: 01.01.1979 in Nizamabad, India

genehmigt durch die Fakultät für Maschinenbau
der Otto-von-Guericke Universität, Magdeburg, Germany

Gutachter : Prof. Dr.-Ing. Martin Heilmaier
Prof. Joachim Röster

Promotionskolloquium am: 12.12.2007

Modelling the influence of microstructure on elastic properties and tensile damage behaviour of Mo-base silicide alloys

Dissertation

Submitted for the academic degree

Doktoringenieur
(Dr.-Ing.)

by: Praveen Goud Biragoni
born on: 01.01.1979 in Nizamabad, Andhra Pradesh, India

Approved from the faculty of Mechanical Engineering
Otto-von-Guericke University, Magdeburg, Germany

Referees: Prof. Dr.-Ing. Martin Heilmaier
Prof. Joachim Röster

Defended on: 12.12.2007

This work is dedicated to my beloved parents and my wife …

Abstract

The enhanced high temperature capabilities of Mo-based silicide multiphase alloys, that can be operated up to 1300°C, have made them possible replacement for the presently used Ni-base single-crystal superalloys for the application in aircraft/rotorcraft engines and in aero-derivative land-based gas turbines. For the applications as high temperature structural materials, the knowledge about their damage behaviour and the temperature dependent elastic properties and their dependence on microstructure is required besides their fracture toughness, creep strength and oxidation resistance.

Micro hardness and global hardness measurements of Mo-based silicide alloys of compositions Mo-8.9Si-7.7B and Mo-2.7Nb-8.9Si-7.7B (both in at. %) were carried out. Tensile testing and three point bending experiments were also conducted for the 2nd alloy to determine the temperature dependent elastic properties and tensile strengths, and fracture toughness at RT respectively.

The effective material properties and the overall behaviour of a composite material depend on the microstructure with regard to the morphological parameters like grain size, volume fraction and arrangement of the reinforcement phase in the matrix. In this dissertation work, Mo-Si-B alloys are studied numerically for the influence of these parameters of intermetallics (Mo_3Si and T2 phases) and Molybdenum solid solution on the overall behaviour of the alloy. Real microstructures and Voronoi structures representing various Mo-Si-B alloy compositions were generated and finite element simulations were performed in ANSYS using numerical homogenization techniques. The results, obtained using the finite element homogenization technique, were compared with different analytical methods and with experimental results that were conducted for few compositions.

Damage and crack growth behaviour of various three phase- and two phase- Mo-Si-B alloy compositions have been simulated based on Element Elimination Technique (EET) using finite element method. In this approach the microstructural simulations were performed based on Voronoi tessellation in which the surface was discretized into polygonal cells and each polygon was assumed as grain. The individual grains in each material phase were assigned different failure stresses as failure criteria, evaluated from the fracture toughness of the phase and their corresponding grain sizes. The influence of grain size and volume fraction of various combinations of the constituent phases on the Tensile strength and plastic failure strains of the Mo-Si-B alloy compositions have been investigated.

The finite element simulations of Mo-Si-B composition were implemented in a FE package called ANSYS. For application of incremental loading for simulation of damage behaviour using Element Elimination Technique, simple and efficient algorithms have been developed in FORTRAN. An object oriented finite element program, PPM2OOF, was used to create FE models. The area fractions of phases in the microstructures were quantified using programming in an image analysis software product called IDL. Algorithms have been developed to create Voronoi structures in MATHEMATICA.

Keywords: Mo-Si-B alloys, Real microstructures, Voronoi structures, Microstructural characterization, Modelling and finite element simulations, Effective material properties, Damage and Crack growth, tensile strength, fracture toughness.

Table of Contents

List of Tables

List of Figures

Nomenclature

F	Load applied by Vickers indenter
d	Arithmetic mean of the two diagonals of Vickers indenter
HV	Vickers hardness
HV_{comp}^{global}	Vickers hardness of composite
$HV_{Mo(ss)}^{micro}$	Vickers hardness Mo(ss) phase
HV_{IM}^{micro}	Vickers hardness of intermetallic phase mixture
V_{Mo}	Volume fraction of Mo(ss) phase
V_{IM}	Volume fraction of intermetallic phases
σ_{cal}	Max stress (obtained from three point bending test)
σ_{YS}	Tensile stress
UTS	Ultimate tensile strength
σ	Stress tensor
ε	Strain tensor
σ_i	Elemental stresses
ε_i	Elemental strains
$\overline{\sigma}_i$	Average stresses
$\overline{\varepsilon}_i$	Average strains
σ_{YS}	Yield stress (obtained from tensile test)
V	Volume of the RVE
$F_{\max}$	Maximum load (from the three point bending test)
S, d and t	dimensions of three point bending test specimen (length, width and thickness)
a	Total notch depth
K_I	Stress intensity factor
K_{IC}	Critical stress intensity factor
a_{cr}	Critical crack length (grain size)

C_{ij}	Stiffness coefficients
C	Stiffness matrix
S	Compliance matrix
E	Young’s modulus
G	Shear modulus
K	Bulk modulus
ν	Poisson’s ratio
E_{11}	Transverse Young’s modulus,
ν_{12}	Transverse Poisson’s ratio,
G_{12}	In plane shear modulus or Transverse Shear modulus
K_{eff}	Effective bulk modulus of the composite material
G_{eff}	Effective shear modulus of the composite material
K_m	Bulk modulus of the matrix
G_m	Shear modulus of the matrix
ν_m	Poisson’s ratio of the matrix
ν_p	Poisson’s ratio of the second phase
K_p	Bulk modulus of the second phase
G_p	Shear modulus of the second phase
K_L, K_U	Lower and upper bounds of bulk modulus of the composite
G_L, G_U	Lower and upper bounds of effective shear modulus of the composite
M_m	matrix modulus
M_p	second phase modulus
V_m	Volume fraction of the matrix
V_p	Volume fraction of second phase

Acknowledgement

Firstly, I would like to thank and sincerely express my deep gratitude to Prof. Dr.-Ing. Martin Heilmaier for his invaluable support, guidance and motivation during my PhD work under his supervision. I am grateful for his openness for accepting and encouraging new ideas in my research work.

I would like to thank Dr. Holger Saage for his kind and selfless help in the initial stage of my research work at the Institute for Materials and Joining Technology.

I would also like to thank Prof. Thomas Böhlke for his effective cooperation and stimulating discussions during my PhD work.

I express my sincere thanks to Dipl.-Ing. Geza Bondar for spending his valuable time in discussions and giving his valuable suggestions.

I would like to thank Prof. Gerhard Mook for his kind help whenever I needed. I thank Gabriele Dietze, Olaf, Metallography Lab staff and other members of the institute for their support during my stay at our Institute.

I would like to acknowledge the funding provided by European commission through ULTMAT Project for my research work.

I would like to thank my mother, family and my fiancée for their unconditional love and support during my stay in Germany.

Last but not the least I would like to thank my friend Dr. Sreedhar Kari for his very useful suggestions and his moral support during my stay at Magdeburg and also I would like to thank all my friends who supported me directly or indirectly during my stay at Magdeburg.

Praveen Goud Biragoni

Chapter 1

Introduction

Increasing the temperature capability of turbine blade materials has been identified as a major requirement to develop efficient and clean aircraft vehicles. Due to their high melting point of around 2000°C Mo-based silicide multiphase alloys are anticipated to possess enhanced high temperature capabilities of up to 1300°C, i.e. 150°C more as compared to the presently used Ni-base single-crystal superalloys [1], for application in aircraft/rotorcraft engines and in aero-derivative land-based gas turbines. The increased temperature capability will allow reduction of specific fuel consumption, CO_2 emissions and cooling air requirement, which will lead to a further increase in efficiency and reduction in component weight.

There has been lot of research on Mo-base silicide alloys for the improvement of their properties most important for high temperature applications such as oxidation resistance, fracture toughness, ductility, and creep strength which mainly depend on the scale and topology of the microstructure, as well as the mechanical properties of the toughening body centered cubic (bcc) Mo(ss) phase. Besides the aforementioned requirements, applications as high temperature structural materials, for example as guide vanes in a turbine environment, also require the knowledge about their damage behaviour, the temperature dependent elastic properties as well as their dependence on microstructure. However, a thorough review of literature reveals that there has been not much numerical analysis done on Mo-base composite materials. It is, therefore, the objective of this thesis to combine an experimental and numerical approach for predicting the elastic properties and the damage behaviour of Mo-Si-B composite materials with varying microstructures.

The application of numerical methods for predicting these properties can significantly reduce the number of time consuming and expensive experiments with laboriously manufactured material samples. This clearly improves the development and design of new materials for modern engineering applications such as aircraft turbine blades.

A concept of homogenization is used for determining the overall properties of the material: this is the important aim of theoretical studies of multiphase materials, namely deducing their overall or effective behaviour (e.g. stiffness, strength properties, thermal expansion and electromechanical properties etc.) based on the knowledge of the material behaviour of the constituents and from the geometrical arrangement of the phases. In general the object under consideration is regarded as a large-scale or macroscopic structure. The common approach to model the macroscopic properties of composites is to create a representative volume element (RVE) or a unit cell that captures the major features of the underlying microstructure. The mechanical and physical properties of the constituent materials are always regarded as a small-scale or microstructural feature. One of the most powerful tools to speed up the modelling process, both the composite discretization and the computer simulation of composites in real conditions, is the homogenization method.

The real and artificial microstructure simulations have been implemented in a finite element software package called ANSYS. Simple and efficient algorithms have been developed in FORTRAN in order to perform a systematic numerical testing of composite microstructures by applying incremental loading. Algorithms have been developed to create Voronoi structures in MATHEMATICA, a high level programming language. An object oriented finite element program, PPM2OOF, was used to create finite element models. The areal fractions of phases in the microstructures were quantified using programming in an image analysis software product called IDL.

Aim and Objectives of this thesis have been:

- To combine an experimental and numerical approach for predicting the elastic properties of Mo-Si-B composite materials with varying microstructures and their dependence on temperature.
- To numerically analyze the effect of volume fraction and grain sizes of different phases in the Mo-Si-B alloys on their damage behaviour, tensile strength and resistance to crack growth at room temperature.

This thesis work is organized in the following way:

After this introductory chapter a literature survey on Mo-Si-B alloys is given in Chapter 2 explaining the need for research on Mo-base silicide alloys and why they are potential materials which could replace the currently used Ni-base alloys for high temperature applications. Besides, the physical and mechanical properties of the constituent phases present in the Mo-base alloy system are presented with a brief explanation of the influence of microstructure on the mechanical properties of Mo-base silicide alloys.

Chapter 3 describes the experimental work done to evaluate the effective properties, tensile strength and fracture toughness of Mo-Si-B alloys as well as the microstructural characterization.

In Chapter 4 the literature review on common existing analytical methods is made. Procedures are explained for real microstructures and Voronoi structure generation and development of finite element model from them to perform simulations. Evaluation of elastic constants and elastic moduli using generalized Hook's Law is explained in detail here.

In Chapter 5 the results obtained from finite element simulations are discussed and a comparison with experimental results and analytical methods is given. Also, a case study is made by improving the properties of the constituent phases and changing their arrangement to show the better accuracy of the numerical analysis as compared to the analytical methods.

Chapter 6 explains the Element Elimination Technique (EET) used to predict the damage behaviour of Mo-Si-B alloys. The influence of grain sizes and volume fractions of individual phases on the tensile strength and crack growth are discussed.

Chapter 7 presents the summary of the thesis and an outlook on the direction for future research that could be done in this field.

Chapter 2

Literature review on Mo-Si-B alloys

2.1 Introduction

In view of their outstanding intrinsic properties, notably the high melting point and, thus, the very good mechanical properties and creep strength at elevated temperatures, refractory metal (RM) silicide alloys are considered first choice replacements for Ni-base superalloys with the aim of increasing the (thermodynamic) efficiency of gas turbine engines [1].

Amongst the RM silicide alloys within the Mo-Si-B system, which consist of a bcc Mo solid solution (Mo(ss)) and the intermetallic phases Mo_3Si and Mo_5SiB_2 (T2), Fig. 2.1, have melting points on the order of 2000°C and, thus, promise potential as ultra-high

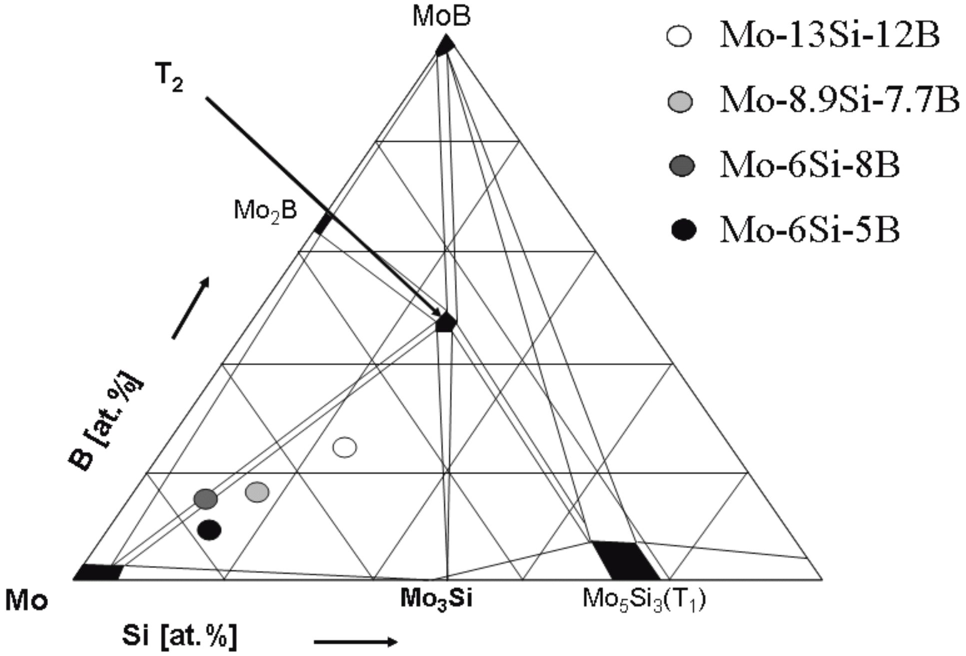

Fig. 2.1 Isothermal section of Mo-Si-B at 1600°C [10].

temperature structural materials. Mo-Si-B alloys can be processed such that the Mo(ss) is present in the form of isolated particles in a silicide matrix, or as a continuous matrix “cementing” individual silicide particles together.

Initially, molybdenum disilicide ($MoSi_2$) has been extensively studied because it has an excellent oxidation resistance at high-temperature (up to 1700 °C). Even though $MoSi_2$ has an advantage over other candidate materials in terms of its outstanding high temperature oxidation resistance due to the formation of a protective silica glass scale, it is very brittle at room temperature with fracture toughness on the order of 3 $MPa\sqrt{m}$ [23] and has a low creep-strength above 1200 °C [2]. Besides, it has poor oxidation resistance at moderated temperature (600–800 °C) because of its ‘pesting behaviour’ [3, 4]. Because of these drawbacks, its brittleness and pesting behaviour, $MoSi_2$ is not suitable as a high-temperature structural material, but is frequently used as heating elements for resistance furnaces. On the other hand, Mo_5Si_3 has a better compressive creep resistance at high-temperatures than $MoSi_2$ [5]. Despite its high creep resistance, Mo_5Si_3 has poor oxidation resistance at high-temperature (>1000 °C) and shows pesting behaviour at moderate temperatures. In addition, Mo_5Si_3 is also very brittle. However, Meyer et al. [6, 7, 8] found that small additions (2 wt.%) of boron to Mo_5Si_3 can dramatically improve the isothermal oxidation behaviour at high-temperatures and can eliminate the pesting behaviour at moderate temperatures (~800 °C). When B is added to the Mo–Si system, Mo, Si, and B can form a ternary phase called T2 with a composition Mo_5SiB_2 [6, 9]. They have studied the isothermal oxidation behaviour of boron-doped Mo_5Si_3 at 800–1600 °C in multiphase alloys of Mo_5Si_3–Mo_3Si–Mo_5SiB_2 (or T1–Mo_3Si–T2). Although T2 is believed to provide good oxidation resistance from the boron-added silica glass scale that forms when it is oxidized, limited experimental data on the oxidation behaviour of T2 exists. Furthermore, because of the problems with brittleness, interest has recently shifted toward the Mo-rich Mo–Si–B alloys which contain Mo as a bcc solid solution. Because of its higher fracture toughness, the presence of the metal phase may help to improve the fracture toughness of multiphase molybdenum silicide intermetallics. As early as 1957, Nowotny et al. [10] pointed out that boron-containing silicides possess high oxidation resistance due to the formation of protective borosilicate glass. A slightly revised version of Nowotny's Mo-Si-B ternary phase diagram based on the work of

Nunes et al. [9] is shown in Fig. 2.1. The strategy for the alloy design is that presence of the bcc-Mo solid solution will provide for ductility and improved fracture toughness of the multiphase alloy while the T2 and Mo_3Si phases will provide Si and B needed to form an oxidation resistant protective scale.

2.2 Physical and mechanical properties of possible constituent phases and elements in Mo-base silicide alloys

It is very important to know the mechanical and physical properties of the constituents of the composites to investigate the overall properties of the alloy. The important properties of the possible phases in Mo-Si-B alloys are reviewed and presented in Table 2.1 and some of the properties of constituent elements are presented in Table 2.2, [11-21].

phases → ***properties ↓***	**Mo solid solution [Mo(ss)]**	**Mo_3Si**	**Mo_5SiB_2(T2)**	**Mo_5Si_3(T1)**
Structure	BCC	Cubic A15	Tetragonal D81	D8m
Melting point (K)	2883	2298	2433-2473	2453
Ductility	Brittle at low temps and ductile at high temps	Brittle	Brittle	Brittle
Brightness	lighter than all phases	Darker than Mo(ss)	Darker than Mo_3Si	Darker than T2 and Mo_3Si
Contribution of the phase in the alloy	imparts fatigue resistance and contributes in creep strength of the alloy at high temperatures	presence of continuous Mo_3Si is detrimental for the room temperature strength	Presence of needles of T2 imparts strength to the alloy	Has excellent creep resistance at temperatures as high as 1400°C
Fracture Toughness (MPa√m)	Poor toughness at ambient temperatures, greater at higher temperatures. Continuous and coarser phase imparts	3	2	At low temps it displays very poor fracture toughness

	more toughness. 7 (for Mo+ 0.5% Si)			
Hardness (GPa)	7.1 (relatively soft)	13 – 13.5	18 – 19 (very strong)	
Oxidation resistance	Gets oxidized at low temperatures (at 550°C to 750°C)			can be susceptible to oxidation problems at ~1000°C
Young's Modulus (GPa) & Poisson’s ratio	298 & 0.30	293 & 0.297	383 & 0.269	260
creep strength	Discontinuous matrix of Mo(ss) imparts better creep strength than that of continuous matrix of Mo(ss)	Mo_3Si is a factor in determining the creep strength		
Density (g/cm^3)	10.22	8.9	8.8	
CTE, α at 25°(K)	$5*10^{-6}$	$3*10^{-6}$	$6*10^{-6}$	
at 1300°(K)	$6*10^{-6}$	$7*10^{-6}$	$8.5*10^{-6}$	

Table 2.1: A review on mechanical and physical properties of the constituent phases in the Mo-base silicide alloys.

elements → ***properties ↓***	**Mo**	**Si**	**B**	**Nb**	**W**
Structure	BCC	Diamond	B12 Icosahedral	BCC	BCC
Melting point	2623°C	1414°C	2075°C	2477°C	3422°C
Density (g/cm^3)	10.2	2.33	2.34	8.57	19.3
Atomic Radius (A°)	1.37	1.1	0.85	1.44	1.38
Effect on the alloy	It is primary element in the alloy, has a high elastic modulus and contributes to the strength of the alloy.	Provides oxidation resistance at high temperatures, at low oxygen partial pressures Si evaporates as SiO to protect Mo.	Boron-containing silicides possess high oxidation resistance due to the formation of protective borosilicate glass	Can improve creep strength more than that of W because of it's more size	Can't improve creep strength as much as that of Nb
Young's Modulus (GPa)	329	47	--	105	411
Poisson's Ratio	0.31	--	--	0.4	0.28
Ductility	more ductile than W	ductile	--	--	ductile

Table 2.2: Review on properties of possible constituent elements in Mo-base silicide alloys.

2.3 Mo-based silicide alloys as a replacement for Ni-based alloys

Currently, Nickel-base superalloys are primarily used in the high temperature range of turbines. These superalloys have outstanding oxidation and mechanical properties at elevated temperatures, but their service temperatures are inherently limited to metal temperatures below 1100°C because of incipient melting phenomena. Hence, sophisticated cooling mechanisms and development of thermal barrier coatings (TBCs) the gas inlet temperatures cannot be significantly increased [1] further with these materials, see Fig. 2.2, by Dimiduk and Perepezko [1]. This emphasizes the need for the new ultra high temperature materials: Oxide dispersion strengthened materials, with solidus temperatures as high as 1480°C [22], can operate above 1100°C. However, their creep strengths are relatively low. For example, the Ni-base ODS alloy MA754 has a 1000 h rupture strength of 78 MPa at 1150°C and the Fe-base ODS alloy MA956 has a 100 h rupture strength of 51 MPa at 1100°C [22]. Also, these ODS alloys exhibit high stress exponents which make them prone to sudden failure in creep since a small increase in stress can result in a dramatic increase in the creep rate. In order to increase the thermodynamic efficiency of fossil energy systems, strong, tough and oxidation resistant materials capable of service temperatures much higher than 1000°C are needed. Hence, the main objective of work on RM silicide alloys is to manufacture a composite material that takes advantage of (i) the beneficial oxidation resistance of the silicides and (ii) the outstanding mechanical properties of refractory metals. While refractory elements such as Nb, Mo, Ta, and W have very high melting points, they lack oxidation resistance.

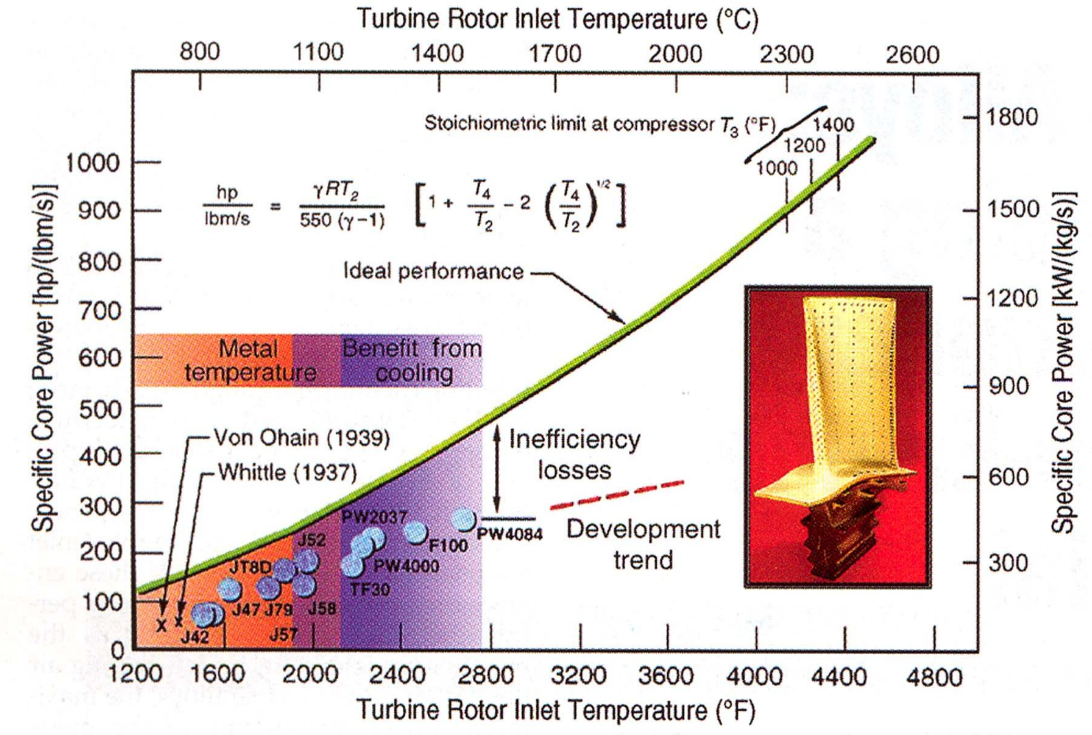

Fig. 2.2 Core power versus turbine inlet temperature for selected gas turbine alloys. (Dimiduk and Perepezko [1]).

Besides $MoSi_2$, which has been reviewed in section 2.1 already, two main alloy systems have been examined to date. In the first one, which was pioneered by Akinc and collaborators [24-26], intermetallic alloys consisting of Mo_5Si_3, the T2 phase Mo_5SiB_2, and the A15 phase Mo_3Si were investigated. These alloys exhibit excellent oxidation resistance at elevated temperatures (e.g. 1300°C) but comparably low fracture toughness and ductility proved to be an obstacle for their usage in turbine rotar hardware. The second system was pioneered by Berczik et al. [27, 28]. Berczik investigated alloys consisting of Mo(ss), Mo_3Si, and T2. While these alloys are not as oxidation resistant as the Mo_5Si_3-T2-Mo_3Si alloys, they contain a ductile bcc phase, Mo(ss). In his approach two manufacturing steps have appeared to be at least problematic to obtain sound material in sufficient quantities at reasonable costs: (1) he employed a rapid solidification (RS) step via Helium gas atomization to obtain a matrix of Mo solid solution for adequate fracture toughness and ductility at temperatures below 600°C with embedded intermetallic compounds Mo_3Si and Mo_5SiB_2 for oxidation resistance due to the formation of a dense borosilicate glass layer on the metal surface, and (2) he also reported that for sound wrought processing temperatures above 1700°C were needed which makes industrial up-scaling hardly feasible. In order to overcome limitation (2) Jéhanno et al, [29] suggested a powder-metallurgical manufacturing route with mechanical alloying (MA) as the technique , also replacing the (costly) RS gas atomization step (1) to economically obtain large quantities of three phase Mo-Si-B material with a nearly continuous Mo solid solution matrix. This material beneficially proved superplastic tensile deformation at temperatures as low as 1300°C, exhibiting an ultrafine microstructure with extraordinary thermal stability.

2.4 Strategies to develop Mo-base silicide alloys

There has been lot of research on Mo-base silicide alloys for the improvement of their properties such as oxidation resistance, fracture toughness, ductility, and creep strength which mainly depend on the volume fraction and distribution of Mo solid solution. In order to improve the required mechanical properties as listed above, mainly the effectiveness of the toughening phase, Mo solid solution, is needed to be taken care of.

Following, some of the ways obtained from literature are presented which can improve solid solution strengthening and ductility of Mo solid solution:

- According to early work of Scruggs, by distribution of spinel-like oxides, which act as repositories for impurities in Mo- and W-base alloys, ductility can be increased [15]. Spinels are a mixture of a metal monoxide and a metal sesquioxide which combine according to the general formula MO.M2O3 (or MM2O4) where the M's may be the same or dissimilar metals. But from recent investigations, Gunter et al. [30] believe that the ductilizing effect may be caused by the associated reduction in grain size, rather than by the actual presence of the spinel particles and therefore controlling the molybdenum grain size, rather than adding spinel particles, should be a way to (i) improve the ductility of monolithic molybdenum alloys and (ii) possibly improve the ductility of the Mo(ss)lybdenum phase in Mo–Si–B alloys.
- Solid solution alloying additions with Nb increase creep strength of the Mo-Si-B alloy [31]. Alloy additions of Nb and W cause solid solution strengthening, but strengthening due to Nb is more pronounced. This can be rationalized by the large Goldschmidt radius of Nb (1.44 Å) as compared to Mo (1.37 Å). Because of its large atomic size Nb may reduce the diffusion coefficients of the various phases, the dislocation mobility, or both. In addition, Nb increases the activation energy for the creep strength dramatically [31].
- The addition of zirconium (Zr) was reported to strengthen grain boundaries in Mo solid solution [32] by reducing the percentage of silicon, which causes embrittlement and changes the fracture mode to intergranular. It was observed that Mo(ss) that possesses 4 at.% Si in solid solution without Zr, has only 3 at.% Si in solid solution if 1.5 at.% of Zr was deliberately added to the alloy. Less Si causes less embrittlement by increasing both, the ductility as well as increases the fracture toughness of the alloy. Work from Sturm et al. [20] also suggests that reduction in Si pct from Mo solid solution below 0.5 % increases its ductility.
- The addition of rhenium (Re) into Mo bcc solid solution markedly lowers the ductile to brittle transition temperature (DBTT) of the bcc phase, resulting in a higher ductility and toughness of Mo-Re alloys [21]. Recent work by Leichtfried

et al. [33] verified by Charpy impact testing that increasing Re additions, from min 5 % to max 41 %, continuously reduce the DBTT to below room temperature. But the disadvantage with Rhenium is that it is heavy, costly and processing of these alloys may become complicated.

2.5 Influence of microstructure on material properties of Mo-base silicide alloys

Microstructure has major influence on the materials properties in terms of grain size, volume fraction and continuity of Mo(ss). Schneibel et al [31, 34, 35] worked on the relationship between the topology as well as scale of the microstructure of Mo-Mo_3Si-Mo_5SiB_2 alloys, and the resulting creep strength and fracture toughness. From these investigations it was observed that the alloy with the microstructure having low volume fraction of discontinuous and fine Mo(ss) matrix offers better oxidation resistance, while creep strength can be improved by achieving a microstructure with low volume fraction of discontinuous and coarse Mo(ss) matrix. At high temperatures a fine microstructure is associated with poor strength due to the presence of a high density of high diffusivity interfaces, which may lead to diffusion controlled deformation, whereas at low temperatures it yields high strength due to limiting the free path of dislocation movement. Depending on its volume fraction and distribution, the Mo(ss) can improve the room and high temperature fracture toughness significantly. Fracture toughness can be improved by obtaining a microstructure with high volume fraction of continuous and coarse Mo(ss) matrix. Microstructures containing Mo_3Si and T2 particles in Mo(ss) matrix were obtained by powder-metallurgical processing. Because of the coarse microstructure and because of inability of the micro-cracks to avoid ductile Mo(ss) particles, these microstructures are associated with significantly improved room temperature fracture toughness values. The microstructure of material obtained by powder metallurgy processing was observed to be coarser than that of the cast and annealed alloys. And the coarser microstructures result in higher ductile phase toughening than fine microstructures. By PM processing, continuous Mo(ss) matrix can be obtained which has the potential for higher ductility and fracture toughness than the corresponding cast material, which consist of continuous brittle matrix.

Chapter 3

Mechanical properties of Mo-Si-B alloys

3.1 Experiments conducted and results

3.1.1 Global and micro hardness measurements

Hardness was measured using a Vickers hardness tester. Two PM alloys have been provided in the frame of the ULTMAT program [72]: (1) the alloy Mo-8.9%Si-7.7%B (all compositions given in at. %) was supplied in hot-worked condition with an extrusion diameter ratio of 3:1, while (2) annealed and non-annealed specimens of a Mo-2.7Nb-8.9Si-7.7B were delivered in a hot isostatically pressed (HIPed) condition. For further details regarding processing see [38].

The Vickers hardness test method consists of indenting the test material with a diamond indenter, in the form of a pyramid with a square base and an angle of 136 degrees between opposite faces subjected to a load of 1 to 100 kgf. In this case a load of 10kgf was applied for 10 seconds. The two diagonals of the indentation left in the surface of the material after removal of the load were measured using a microscope and their average was calculated. The area of the sloping surface of the indentation is calculated. The Vickers hardness is the quotient obtained by dividing the kgf load by the square mm area of indentation:

$$HV = \frac{2F\sin\frac{136^\circ}{2}}{d^2} \approx 1.854\frac{F}{d^2} \tag{3.1}$$

F = Load in kgf

d = Arithmetic mean of the two diagonals in mm

HV= Vickers hardness

The measured hardness of Mo-8.9%Si-7.7%B alloy was 1025 HV10, which is equivalent to 10 GPa [to convert HV to GPa multiply by 0.009807 [74]]. Hardness of Mo-8.9%Si-7.7%B alloy was found to be around one third higher than that of Mo-2.7Nb-8.9Si-7.7B alloy and there was slight decrease in the hardness (see table 3.1) after annealing the sample at 1700°C for 5 hrs.

The micro hardness of the Mo(ss) matrix and intermetallics was measured using a Vickers micro indenter. Metallographic preparation was made on the surface of the alloy specimen. After the specimen was ground with emery wet paper followed by diamond polishing with 3μm diamond suspension, it was etched with a solution containing 75ml H_2O, 25ml HCl, 8g $FeCl_3$. An attempt to etch the specimen with Murakami's reagent ($K_3Fe(CN)_6$ 10 grams, KOH 10 grams, Water 100 ml), was not successful. The microstructure consisted of continuous Mo(ss) matrix with dispersed intermetallic particles (see fig. 3.1). The intermetallic particles (Mo_3Si and Mo_5SiB_2) were not distinguishable. Indentations were made with loads of 0.02 kgf. The hardness of Mo(ss) matrix and intermetallic phase mixture were found to be 733.9 HV 0.02 i.e. 7.2 GPa and 1484.3 HV 0.02 i.e. 14.6 GPa respectively, see Table 3.1.

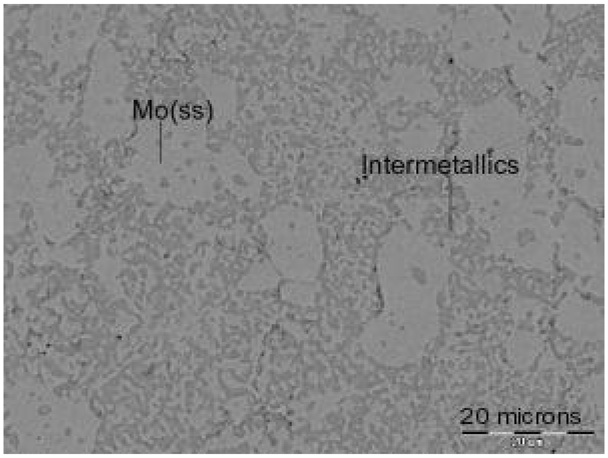

Fig. 3.1 SEM micrograph of the alloy Mo-8.9%Si-7.7%B.

The microstructure was quantified for volume fractions of phases, using IDL as explained in subsequent section, and the global hardness obtained from the micro hardness of Mo(ss) matrix and intermetallics was compared with the rule of mixtures. From the rule of mixtures,

$$HV_{comp}^{global} = V_{Mo}\, HV_{Mo}^{micro} + V_{IM}\, HV_{IM}^{micro} \qquad (3.2)$$

by substituting the volume fractions, V_{Mo} = 0.61 and V_{IM} = 0.39, and micro hardness values in equation 3.2, yields a macro hardness of 10 GPa which is equal to the measured global hardness value, Table 3.1.

material	Mo-8.9Si-7.7B			Mo-2.7Nb-8.9Si-7.7B	
	Global hardness	micro hardness		Annealed (at 1700°C for 5 hrs)	Non-annealed
		Mo(ss)	intermetallics		
Hardness (GPa)	**10**	**7.2**	**14.6**	**6.9**	**7.6**

Table 3.1: Hardness values of the alloys measured by Vickers indenter.

3.1.2 Testing methods for elastic properties

3.1.2.1 Tensile testing

Round tensile specimens of gage length 12.5 mm and diameter 4.95 mm at the center were machined from the alloy Mo-2.7Nb-8.9Si-7.7B. Tensile tests were carried out between RT and 650°C on a computer controlled MTS-tensile testing setup (see fig.3.2) with force capacity of 100 KN to determine the elastic properties and strength values. The specimens were tested at a constant displacement rate of $1.25 \cdot 10^{-3}$ mm/s. This corresponds to an engineering strain rate of $1 \cdot 10^{-4} s^{-1}$. The strain was measured using a contact extensometer that was mounted on the specimen. The extensometer had a gage length of 12.5 mm and a range of 1mm strain. For the tests at higher temperatures the heating rate of the specimen was maintained at 5 K/s and after reaching the set point the holding time was 5 seconds. Comparison of tensile test results on Mo-3%Si-%Nb-1%B HIP alloy can be seen in table 3.2. Values for ultimate tensile strength UTS and Young's modulus E in the temperature range between RT and 600°C are mean values of at least 3 samples (except at 650°C). In this case, only 2 samples were tested. The elastic moduli show the usual trend of decreasing values with increasing temperature.

Fig. 3.2 MTS-tensile testing setup.

Test temperature	UTS [MPa]	E [GPa] from Tensile testing
RT	405	349
300°C	266	341
600°C	332	328
650°C	443	320

Table 3.2: Comparison of tensile test results on Mo-2.7Nb-8.9Si-7.7B HIPed alloy in temperature range between RT and 650°C.

3.1.2.2 Dynamic resonance method

A dynamic resonance method was applied utilizing an ELASTOTRON 2000 device (company HTM Reetz, Berlin) equipped with a high temperature vacuum furnace. Specimens were tested in form of bars with rectangular cross section of dimensions 100 mm (longitudinal, *l*) x 8 mm (long transverse, *lt*) x 4 mm (short transverse, *st*). Three samples of the quaternary alloy Mo-2.7Nb-8.9Si-7.7B were tested to get additional information about homogeneity of the material. These samples were attached to a sender – receiver system consisting of piezoelectric actuator and sensor, respectively, by carbon fiber wires as sketched in Fig. 3.3. For determination of Young’s modulus *E*, the sample is tilted by an angle of 45° with respect to the horizontal axis (Fig. 3.3(a)). Torsional vibrations can be forced using the set-up shown in Fig. 3.3(b), which is used for determining the shear modulus *G*.

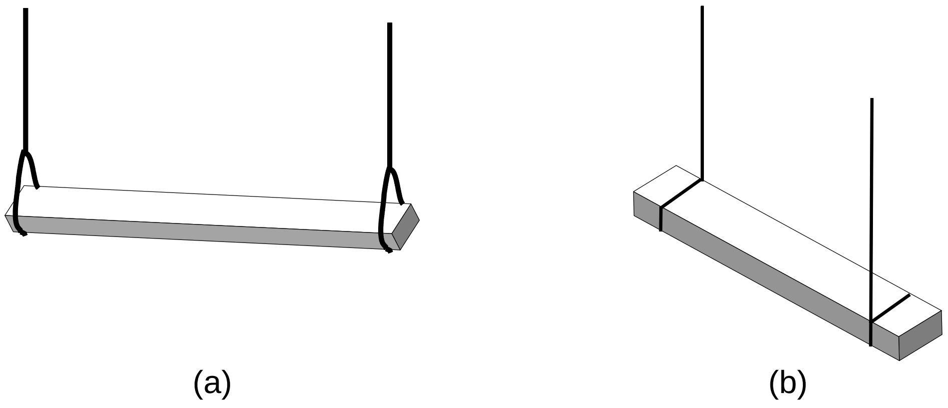

Fig. 3.3 Fixture of samples by carbon fiber wires for determining: (a) the Young's modulus E; (b) the shear modulus G.

Calculation of *E* was carried out according to [36] where the transversal resonance frequencies up to the 6th order were taken into account. The shear modulus G was determined in accordance with European standard EN 843-2 (2005-01) [37].

With the fixture shown in Fig. 3.3(a) one is able to excite oscillations in the sample in long and short transverse direction simultaneously within one experiment. Therefore, one measurement is sufficient to determine the Young's modulus independently in two macroscopic directions. A comparison of both results may indicate possible effects from crystallographic texture of the specimens investigated which was, however, not the case here.

3.1.2.3 Influence of annealing on elastic properties

Annealed (at 1700°C for 5 hrs) and non-annealed specimens of the Mo-2.7Nb-8.9Si-7.7B alloy were tested to determine elastic modulus E, shear modulus G and Bulk modulus K in dependence of temperature from RT to 1315°C using the dynamic resonance method as explained in the previous section. Fig. 3.4 shows a comparison between the elastic properties of annealed and non-annealed alloys. The annealed material with a coarser microstructure than that of the non-annealed one by approximately one order of magnitude [38] was observed to have almost identical elastic properties with a negligible difference of less than 2% between both microstructural states indicating that the elastic properties of the material can be considered independent of the sizes of the phases. This is also proved by numerical simulations, which is explained in detail in Chapter 5.

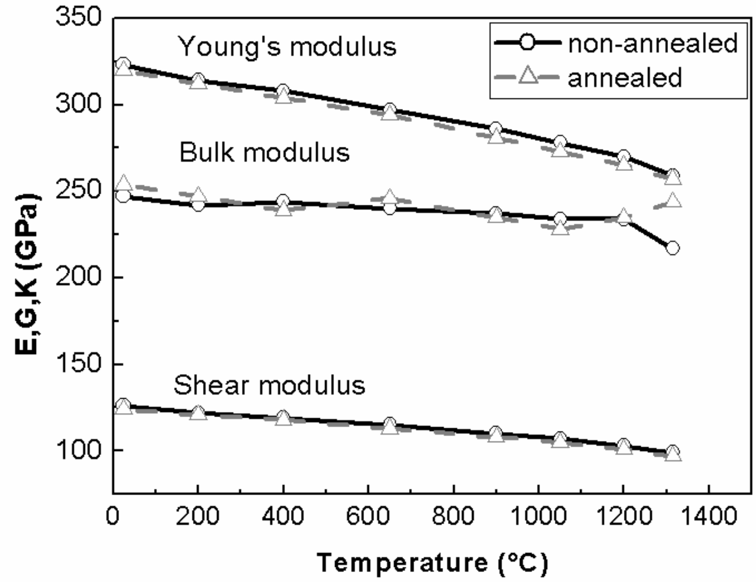

Fig. 3.4 Elastic properties of annealed and non-annealed specimens of the alloy Mo-2.7Nb-8.9Si-7.7B at temperatures between RT and 1350°C.

3.1.3 Fracture toughness from three point bending test

Annealed specimens (at 1700°C for 5 hrs), without a notch, and non-annealed specimens, which were Charpy V-notched, of the alloy composition Mo-2.7Nb-8.9Si-7.7B were subjected to three point bending test at room temperature to evaluate fracture toughness. An electromechanical device ‘TIRA test 2425’ was used for quasi-static 3 point bending.

3.1.3.1 Procedure

Dimensions of the bend bars of non-annealed and annealed alloy, with rectangular cross section and a Charpy V-notch at the mid-length, were 40x10x10 mm. As the material was too brittle to produce a pre-fatigue crack it was subjected to wire EDM method (electrical discharge machining). EDM works by eroding material in the path of electrical discharges that form an arc between an electrode tool and the work piece. A straight slot is cut along the V-notch by using an electric discharge wire (this can also be done by feeding a circular cutter through the specimen) and this straight slot which is uniform in size across the specimen acts as a crack. Length of this artificially produced slot is 1mm and length of the notch being 2 mm. So the total length of the region including V-notch and the slot is 3 mm.

Gage contacts of 'TIRA test 2425' set up are moved and fixed apart with a 40 mm distance between them which is length of the specimen. The specimen is placed symmetrically on the gage contacts of the set up such that the notch, facing downwards, lies exactly in the middle of the gage contacts. The speed of the central rod is maintained at 0.01 mm/min. Crack opening is performed in mode-I manner which is opening or tensile mode where the crack surfaces move directly apart. As the thickness of specimen is very large with respect to the crack length, the stress intensity factor for mode-I is often called the plane strain "Fracture Toughness". The maximum load to failure is the minimum data required to calculate the fracture toughness. However for making complete evaluation of the specimen behaviour, a plot of load versus displacement is made as exemplified in Fig.3.5.

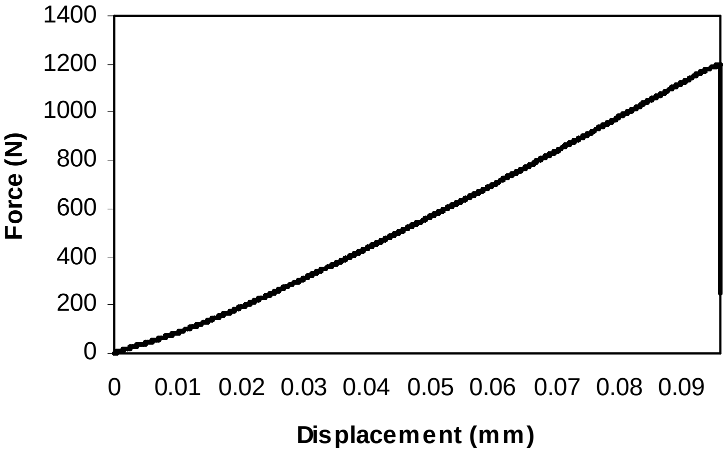

Fig. 3.5 Force-Displacement curve obtained from three point bending test of Mo-2.7Nb-8.9Si-7.7B alloy at RT.

3.1.3.2 Evaluation and results

From Richard [39] and Brown & Srawley [40] the following equation (3.3) is used for calculating the fracture toughness of the material:

$$\frac{K_I}{\sigma_{cal}\sqrt{\pi a}} = \frac{1}{1-\frac{a}{d}}\sqrt{\frac{A+B\frac{a}{d-a}}{1+C\frac{a}{d-a}+D(\frac{a}{d-a})^2}} \tag{3.3}$$

$$\sigma_{cal} = \frac{3F_{\max}s}{2d^2t} \tag{3.4}$$

Where σ_{cal} = max stress (calculated)

$F_{\max}$ = maximum load (from the test)

s = length of the specimen = 40mm

d = width of the specimen = 10mm

t = thickness of the specimen =10mm

a = total notch depth = 3mm

K_I = stress intensity factor

Regarding the relative crack length, the validity range of Richard's formula, equ. (3.3) for three point bending test specimen is $0 \le \frac{a}{d} \le 0.6$. The coefficients A, B, C and D from the above formula depends on the s/d value, here s/d=4 for the specimen under test, for which the values are

A = 1.19

B = 2.17

C = 7.72

D = -1.9

Three specimens of similar compositions were tested under identical conditions (at room temperature) and their fracture toughness values, calculated from the above formula, are listed in Table 3.3.

	Specimens	**F**$_{max}$ (N)	σ_{cal} (MPa)	**K$_I$** (MPa√m)	Average **K$_{Ic}$** (MPa√m)
Non-Annealed	1	1269.8	76.2	**7.7**	**7.4**
	2	1169	70.1	**7.1**	
	3	1198	71.9	**7.3**	
Annealed	1	952	57.1	**5.8**	**5.9**
	2	964	57.8	**5.9**	

Table 3.3: Fracture toughness values of non-annealed and annealed Mo2.7Nb8.9Si7.7B alloy.

In order to check whether the specimen has deformed in plane strain condition or not the following condition has been applied:

$$\text{a, t, (d-a)} \geq 2.5\left[\frac{K_I}{\sigma_{YS}}\right]^2 \tag{3.5}$$

The above condition satisfies to prove that the material has deformed under plane strain condition, e.g. assuming σ_{YS} = 385 MPa (obtained from tensile testing) and K_I = 7.1 MPa√m yields a value of 0.85 mm for the right hand side of equ. (3.5), this is substantially lower than all relevant specimen dimensions, namely a, t and (d-a). Hence, the K_I value is critical i.e. $K_I = K_{IC}$.

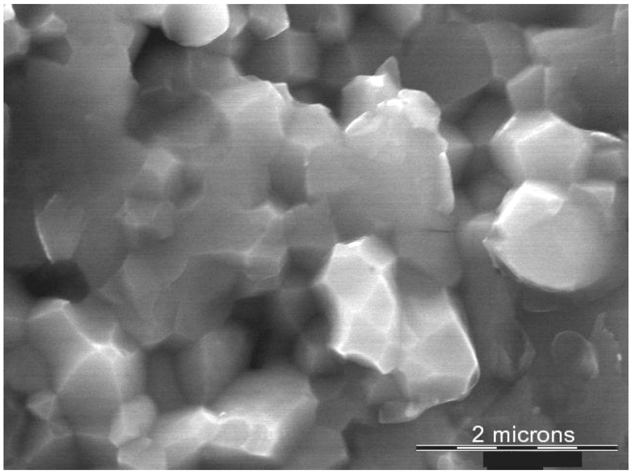

Fig. 3.6 SEM micrograph of Fracture surface of Mo-2.7Nb-8.9Si-7.7B alloy, indicating intergranular brittle fracture.

Annealing of the alloy at 1700°C for 5h did not show any improvement in fracture toughness. In fact, slightly reduced values of around 6 MPa√m were found as compared with the non-annealed material for which the graph between force and displacement is exemplarily shown for the specimen with a fracture toughness of **7.3**MPa√m in fig. 3.5.

The fractured surface of the alloy, observed under the SEM, supports the evaluated low toughness values: it reveals no evidence of ductile fracture at ambient temperatures. Instead, fully intergranular fracture is obvious in Fig. 3.6.

3.2 Microstructural characterization of Mo-Si-B alloys

The microstructures of the samples were characterized by scanning electron microscopy (SEM) combined with energy dispersive X-ray microanalysis (JEOL 6400 SEM and FEI XL30 FEG equipped with EDX and EBSD). Four different alloy compositions and manufacturing routes were considered for subsequent modelling: besides the two PM alloys described already in section 3.1.1, two cast alloys, Mo12Si8.5B and Mo12Si10Nb8.5B, were adopted from literature, Schneibel et al. [11]. The microstructures of these alloys are shown in Chapter 5, fig. 5.1. The area fractions of phases in the microstructures were quantified using programming in an image analysis software product called IDL (Interactive Data Language) [41], by separating the phases as shown in the fig. 3.7.

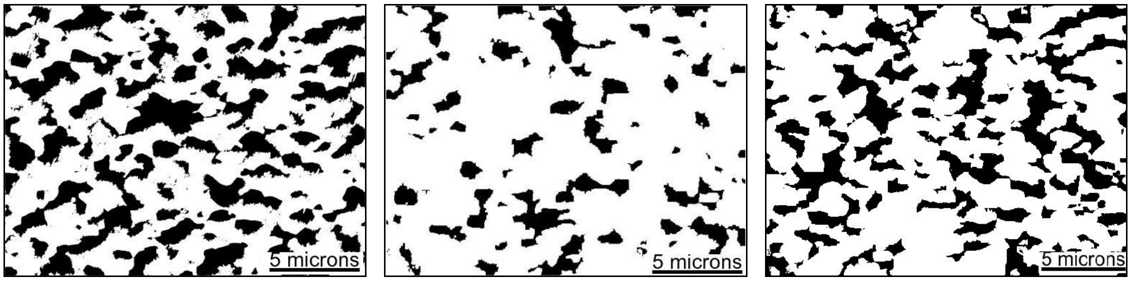

(a) (b) (c)

Fig. 3.7 Separation of phases in Mo-2.7Nb-8.9Si-7.7B by thresholding, (a) Mo(ss), (b) Mo_3Si and (c) Mo_5SiB_2(T2) phase.

Steps involved in microstructure quantification using IDL are:

- Capturing images from SEM or optical microscopy.
- Finding the range of grey values of different phases in the microstructure.
- Thresholding the images for individual phases.
- Creating panoramic images from the thresholded images.
- Coding to measure the area fraction and average grain size of each phase and to plot histograms.
- If the image is not clear to distinguish between the phases it is better to follow line intersection method manually or using analyser software

Quantification of Voronoi structures

Several Voronoi structures of two phase and three phase compositions, representing Mo-Si-B alloys, have been generated for finite element simulations. The size of Voronoi structures generated was 100x100 μm^2 for simulation of elastic properties. Due to the considerably inhomogeneous distribution of Voronoi cells there was a need to slightly re-adjust the composition of the structures generated from MATHEMATICA, a software package [51]. This adjustment was made using IDL programming. And for damage analysis the Voronoi structure of the same size with around 120 grains was generated. Each Voronoi cell in the structure is considered as an individual grain of the corresponding phase and it was manually selected and was assigned one of the phases such that eventually the volume fractions of individual phases make the composition of interest. During and after the distribution, the composition was checked using IDL programming for the volume fractions of individual phases and adjusted accordingly. As the individual grain size plays important role in damage analysis, the grain size distribution is made for individual phases (see fig. 3.8 for example).

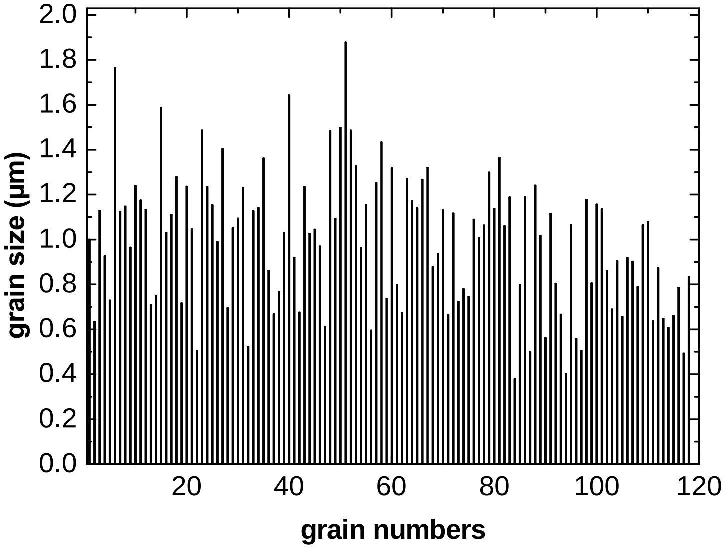

(a)

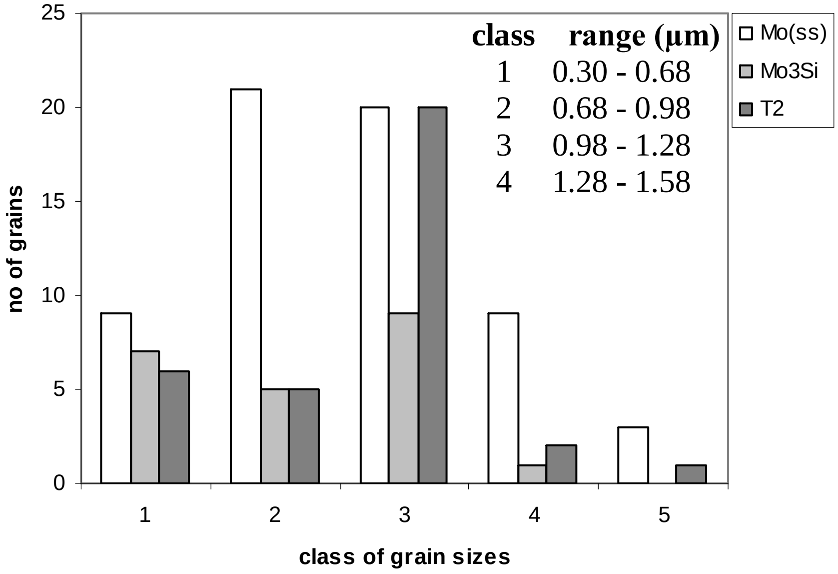

(b)

Fig. 3.8 Grain size distribution of (a) overall grains and (b) each phase in the Voronoi structure of 55%Mo(ss)-15%Mo_3Si-30%T2 alloy composition of 1µm average grain size.

Chapter 4

Modelling and simulation

In this chapter details about existing analytical models, which have been used for comparison with simulation results, are presented. Also various steps involved in creation of geometric model and simulation procedure are discussed. A concept of homogenization is used for determining the overall properties of the material. One of the most powerful tools to speed up the modelling process, both the composite discretization and the computer simulation of composites in real conditions, is the homogenization method.

The aim of the homogenization process is to provide data, which can be used to find a material model for the effective material, and to identify the parameters introduced in this material model. The effective material is supposed to represent the macroscopic properties of the micro heterogeneous material. Until some days ago, homogenization and the determination of effective material parameters could only be done either by performing experiments and tests with the existing material sample or by applying analytical or semi-analytical methods making rather strong assumptions on the mechanical field variables or on the microstructure of the material. The numerical methods can significantly reduce the number of time consuming and expensive experiments with laboriously manufactured material samples. This clearly improves the development and design of new materials for modern engineering applications.

4.1. Review on some existing analytical methods

The development of homogenization techniques for the purpose of predicting the effective material behaviour of modern composite materials is an ongoing process. Many analytical and numerical techniques have been developed to evaluate the effective material properties of different types of composites. Some techniques are mentioned briefly in the following sections.

4.1.1 Voigt and Reuss bounds

The Voigt approximation [42] is one of the simplest models used to evaluate the effective properties of composites and it was originally introduced to estimate the average elastic constants of polycrystals. In this approach it is assumed that the strain throughout the bulk materials is uniform. The inverse assumption to Voigt is the Reuss approximation [43], which assumes that the stress is uniform throughout the phases. The Voigt (arithmetic mean) and Reuss (harmonic mean) bounds are the most elementary bounds on elastic moduli. In terms of isotropic bulk and shear moduli, these bounds can be expressed as

Voigt bounds

$$K_U = K_m * V_m + K_p * V_p \tag{4.1}$$

$$G_U = G_m * V_m + G_p * V_p \tag{4.2}$$

Reuss bounds

$$\frac{1}{K_L} = \frac{V_m}{K_m} + \frac{V_p}{K_p} \tag{4.3}$$

$$\frac{1}{G_L} = \frac{V_m}{G_m} + \frac{V_p}{G_p} \tag{4.4}$$

Where

V_m = Volume fraction of the matrix,

K_m = Bulk modulus of the matrix,

G_m = Shear modulus of the matrix,

V_p = Volume fraction of the second phase,

K_p = Bulk modulus of the second phase,

G_p = Shear modulus of the second phase,

K_L, K_U = Lower and upper bounds of bulk modulus of the composite, and,

G_L, G_U = Lower and upper bounds of effective shear modulus of the composite.

4.1.2 Hashin -Shtrikman bounds

Using variational principles, Hashin [44] and Hashin-Shtrikman [45] established bounds on isotropic and homogeneneous multiphase materials of arbitrary phase geometry. This approach involves the application of the minimum complementary energy principles or minimum potential energy to set the lower and upper bounds for the elastic moduli. When the ratios between the different phase moduli are not too large the bounds derived are close enough to provide a good estimate for the elastic moduli. For the particulate isotropic composite materials, these lower and upper bounds can be written as

$$K_L = K_p + \frac{V_m}{\frac{1}{K_m - K_p} + \frac{3V_p}{3K_p + 4G_p}} \tag{4.5}$$

$$G_L = G_p + \frac{V_m}{\frac{1}{G_m - G_p} + \frac{6(K_p + 2G_p)V_p}{5G_p(3K_p + 4G_p)}} \tag{4.6}$$

$$K_U = K_m + \frac{V_p}{\frac{1}{K_p - K_m} + \frac{3V_m}{3K_m + 4G_m}} \tag{4.7}$$

$$G_U = G_m + \frac{V_p}{\frac{1}{G_p - G_m} + \frac{6(K_m + 2G_m)V_m}{5G_m(3K_m + 4G_m)}} \tag{4.8}$$

Where $K_p > K_m; G_p > G_m; V_p + V_m = 1$

4.1.2 Halpin-Tsai

The Halpin-Tsai equations [46] are a set of empirical relationships that enable the property of a composite material to be expressed in terms of the properties of the matrix and reinforcing phases together with their proportions and geometry. Halpin and Tsai showed that the property of a composite M could be expressed in terms of the corresponding property of the matrix M_m and the reinforcing phase M_p using the following relationships.

Halpin-Tsai Equations:

$$\frac{M}{M_m} = \frac{1+\xi\eta V_p}{1-\eta V_p} \tag{4.9}$$

where

$$\eta = \frac{(M_p / M_m) - 1}{(M_p / M_m) + \xi} \tag{4.10}$$

in which

M = Composite material modulus E(Young's modulus of the composite), G_{LT} (Longitudinal Shear modulus of the composite), or ν(Poisson's ratio of the composite)

M_p = Corresponding second phase modulus E_p, G_p, or ν_p

M_m = Corresponding matrix modulus E_m, G_m, or ν_m

V_p = Volume fraction of second phase

ξ is a measure of second phase of the composite material and is dependent on the geometry of second phase, arrangement of particles, and the type of test (on the modulus considered).

Generally the following values are considered for ξ,

$\xi = 2$ for determining the modulus E_T (Transverse Young's modulus)

$\xi = 1$ for determining the modulus G_{LT} (Longitudinal shear modulus)

4.1.4 Self -consistent method

Predictions of macroscopic properties of two-phase solid composites have mostly been restricted to stating universal bounds on various overall elastic moduli [45]. Such bounds depend only on the relative volumes and do not reflect any geometry, except when one phase consists of continuous aligned fibers [49]. However, when one phase is a dispersion of ellipsoidal inclusions, not necessarily dilute, a much more direct approach is available. This is the self -consistent method originally proposed for aggregates of crystals by Hershey [50] and Kröner [48] and then reviewed and elaborated for composite materials by Hill [47].

The method draws on the familiar solution to an auxiliary elastic problem. In particular, it assumes that interaction of phases is accounted for by imaging each phase to be an inclusion embedded in a homogeneous medium that has the overall properties (*C*, *S*) of the composite. To proceed, denote here the matrix and the other phase by subscripts *m* and *p* respectively. From the elementary relations between the phase and the overall averages of stress:

$$V_p(\overline{\sigma}_p - \overline{\sigma}) + V_m(\overline{\sigma}_m - \overline{\sigma}) = 0 \tag{4.11}$$

The basic postulate of the Self-consistent method suggests that

$$(\overline{\sigma}_p - \overline{\sigma}) = C^*(\overline{\varepsilon} - \overline{\varepsilon}_p) \tag{4.12}$$

$$(\overline{\sigma}_m - \overline{\sigma}) = C^*(\overline{\varepsilon} - \overline{\varepsilon}_m) \tag{4.13}$$

Evidently, both the phases are regarded on the same footing (concentration factors for both the inclusion and the matrix are derived from the same C^*). It means that the same overall moduli are predicted for another composite in which the roles of the phases are reversed. Then, eqs. (4.12) and (4.13) can be rearranged as

$$(C^* + C_p)\overline{\varepsilon}_p = (C^* + C_m)\overline{\varepsilon}_m = (C^* + C)\overline{\varepsilon} \tag{4.14}$$

These self-consistent approximations have been found to generate excellent effective properties at low concentrations of the dispersed phases. However, at high concentrations when the modulus difference between the phases is large, these methods do not perform well. For particulate composite containing a dispersion of elastic spheres or ellipsoids, the self consistent scheme leads to two equations for K_{eff} and G_{eff} which have to be solved iteratively [47]. These are:

$$K_{eff} = K_m + \frac{V_p K_{eff}(K_p - K_m)}{K_{eff} + \left[\frac{3K_{eff}}{3K_{eff} + 4G_{eff}}\right](K_p - K_{eff})} \tag{4.15}$$

$$G_{eff} = G_m + \frac{V_p G_{eff}(G_p - G_m)}{K_{eff} + \left[\frac{16K_{eff} + 12G_{eff}}{15K_{eff} + 10G_{eff}}\right](G_p - G_{eff})} \tag{4.16}$$

Where

K_{eff} = Effective bulk modulus of the composite material,

G_{eff} = Effective shear modulus of the composite material,

K_m = Bulk modulus of the matrix material,

K_p = Bulk modulus of the other phase,

G_m = Shear modulus of the matrix,

G_p = Shear modulus of the other phase,

V_p = Volume fraction of the other phase

4.2. Numerical analysis

4.2.1. Real microstructure generation

Real microstructures of few alloys, as explained in section 3.2 in this Chapter, have been generated to create geometric models and conduct finite element simulations for evaluating elastic material properties.

4.2.2. Voronoi structure generation

Two-dimensional Voronoi structures of different compositions have been produced by programming in ‘Mathematica’ software package [51]. It is a computer algebraic system and also a high level programming language. Using this program algorithms have been developed to create Voronoi structures containing three different phases. As the original microstructure of the material is homogeneous throughout, these structures can be called as RVEs (Representative volume elements). Generation of the RVEs took about 30 mins to 10 hrs depending on the number of Voronoi cells in the structures. The matrix Mo(ss) and the intermetallic phases Mo_3Si, T2, in the Voronoi structures, were assigned with white, light grey and dark grey colours respectively as shown in the Fig. 4.1(a) and (b).

For each of seven different compositions of Voronoi diagrams, representing Mo-Si-B alloys, five structures of varying fineness with 100, 500, 1000, 2000 and 3000 cells (grains) in each structure have been produced. Voronoi structures, of a particular composition with varying RVE size, were produced to observe the effect of RVE size on effective properties.

4.2.3. FEM model creation

Finite element modelling of the real microstructures and Voronoi structures was done in PPM2OOF software package [52], which was downloaded from the site http://www.ctcms.nist.gov//oof/, executed on Linux platform. This is an object oriented finite element program. The process of using ppm2oof can be broken up conceptually into two separate phases, although the actual pieces can be sometimes intertwined. The first phase consists of identifying features in the image and the assigning material properties to them. The second phase consists of creating and refining the finite element mesh.

4.2.3.1. Identifying features

The object of phase one is to assign a material type to every pixel in the image, and, optionally, to assign pixels to *pixelgroups*. Pixels may belong to more than one group, but may not have more than one material.

Most of the operations used in this phase work on the set of currently *selected* pixels. Although ppm2oof can work on many images at once, the set of selected pixels is shared among all the images. The ‘select’ dashboard contains tools for selecting pixels. The */pixelgroups* menu holds commands for assigning the selected pixels to groups. These groups can later be re-selected with the */select menu*, which also contains commands for modifying the currently selected set. Material properties are assigned to the selected pixels with the */materials* menu. Information about the pixels in an image, including their groups and materials, may be obtained from the Pixel dashboard. The Display and Coordinates dashboards control what is drawn in a graphics window and how much of the image is visible.

Some selection operations may work better on modified images. The *Modify_Image* dashboard contains simple tools for image manipulation. The modified images can be saved and restored from the *Image_Gallery* dashboard. If it is necessary to modify an image in an external program, the */ppmfile* command can be used to load a new ppm file, as long as the modified image is the same size as the original.

When working on an image, it is often desirable to restrict all operations to a specified region of the image. The *active_area* menu allows one to define the active area, and store and retrieve it for later use.

4.2.3.2. Mesh generation

In phase two of using ppm2oof a finite element mesh is created from the material image. There are two menus for creating meshes: */simple_mesh* and */adaptive_mesh*. The simple mesh divides each pixel into two triangular elements. This is quick and easy, but it has two flaws. It creates too many elements in regions where a few large elements would suffice, and it creates meshes that resolve all of the details of an image, including pixelization artefacts. Meshes created by the adaptive mesh menu, on the other hand, have large triangles in large homogeneous regions. The edges of the elements follow material and group boundaries, and by choosing the element size one can control which features of the image are resolved by the mesh. The Mesh dashboard provides information about the mesh and lets one select triangles and move nodes manually.

Thus, with this program corresponding properties for different phases were assigned and the two dimensional meshes were generated where triangular elements reproduced different phases in the microstructures.

The meshes along the interfaces of the phases were more refined in order to increase the accuracy. The output file generated by PPM2OOF with general file name ‘*.py’ was converted in to ANSYS input file by a user defined FORTRAN program. During this conversion the 2D triangular meshes were converted into 6-noded wedge elements, which are equivalent to ‘plane 2’ elements in ANSYS, with a constant thickness to obtain a 3D simulation. The finite element model of the microstructure of the alloy Mo-2.7Nb-8.9Si-7.7B can be seen in Fig. 4.1(c).

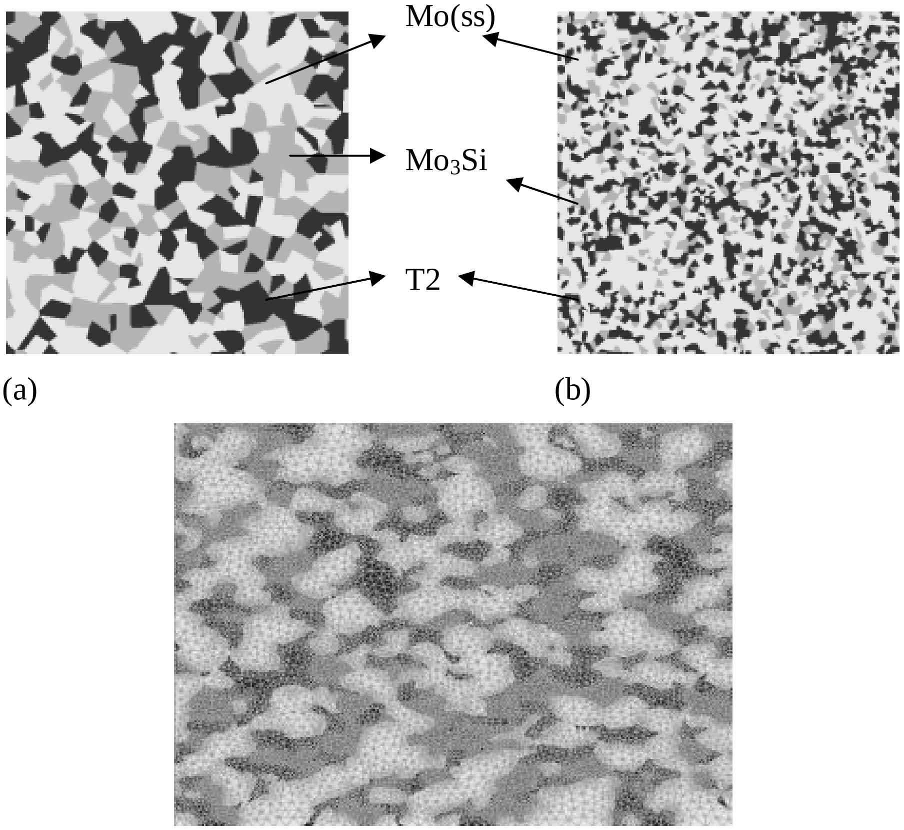

(a) (b)

(c)

Fig. 4.1 (a) Voronoi structure with 500 grains, (b) Voronoi structure with 3000 grains representing 40%Mo(ss)-30%Mo_3Si-30%T2 alloy and (c) meshed (FEM model) real microstructure of Mo-2.7Nb-8.9Nb-7.7Si alloy.

4.2.4. Simulation procedure

The geometric model developed in PPM2OOF is imported into ANSYS where simulations were conducted. Numerical homogenization technique was applied to different RVEs of each composition, which were subjected to uniaxial tensile as well as shear deformation along the two axes of coordinates. A program has been developed, which links the user defined FORTRAN algorithms with the ANSYS program. The FORTRAN algorithms generate the required files, which should be used by ANSYS to evaluate the effective material properties of the given composite. The flow chart shown in Fig. 4.2 gives a clear idea about the steps involved from beginning to the end of evaluation of effective material properties using finite element simulation.

Geometric modelling

- Generate Voronoi structure in MATHEMATICA by user defined program or real microstructure from SEM
- Export the image in to PPM2OOF
- Assign material properties to different phases based on their grey values
- Meshing (with repetition of annealing and refining at the interfaces of the phases for accuracy).
- Converting the above generated geometric model file in to ANSYS readable file by user defined FORTRAN program.

⇕

FE simulation in ANSYS

- Read the input file describing the geometry of RVE generated as above
- Adjust the volume fractions of phases in case of errors from Voronoi cell generation or meshing.
- Apply mixed boundary conditions manually
- Solve the boundary value problem for each coefficient
- Evaluate the appropriate volume averages and evaluate the effective material coefficients

Fig. 4.2 Flow path for the evaluation of effective material properties.

The FEM simulations offer the advantages of a simple and accurate modelling of the existing structure, as well as the possibility for a clear results representation by simultaneously varying several influencing parameters.

4.2.5 Hooke's law and Average theorems

The stress and strain fields in an elastic medium are related by generalized Hooke's Law [53] by introducing either stiffness constant C_{ij} or compliance constant S_{ij}. The relation between $\overline{\sigma}_i$ and $\overline{\varepsilon}_i$ determine the constitutive law. In the linear elasticity case the relation can be written in the following matrix form:

$$\begin{bmatrix} \sigma_{11} \\ \sigma_{22} \\ \sigma_{33} \\ \sigma_{23} \\ \sigma_{31} \\ \sigma_{12} \end{bmatrix} = \begin{bmatrix} C_{11} & C_{12} & C_{13} & C_{14} & C_{15} & C_{16} \\ & C_{22} & C_{23} & C_{24} & C_{25} & C_{26} \\ & & C_{33} & C_{34} & C_{35} & C_{36} \\ & & & C_{44} & C_{45} & C_{46} \\ & & & & C_{55} & C_{56} \\ & & & & & C_{66} \end{bmatrix} \begin{bmatrix} \varepsilon_{11} \\ \varepsilon_{22} \\ \varepsilon_{33} \\ \varepsilon_{23} \\ \varepsilon_{31} \\ \varepsilon_{12} \end{bmatrix} \tag{4.17}$$

Or in a condensed form as:

$$\overline{\sigma}_i = C_{ij}\overline{\varepsilon}_j \qquad i, j = 1,...,6 \tag{4.18}$$

$$\overline{\varepsilon}_i = S_{ij}\overline{\sigma}_j \qquad i, j = 1,...,6 \tag{4.19}$$

Through homogenization, the composite specimen is regarded as a body of an effective homogeneous material, whose mechanical behaviour is described by a constitutive law. This constitutive law can be determined based on the detailed fields in the RVE through an "averaging" procedure. It is assumed that the average mechanical properties of the RVE are equal to the average properties of the corresponding composite alloy [54]. If the micro stresses, σ_i and micro strains, ε_i are known under the applied load, the average stresses and strains over the RVE are defined by equation (4.19) and (4.20).

$$\overline{\sigma}_i = \frac{1}{V}\int_V \sigma_i(x_k)dV, \qquad i = 1,\ldots,6 \tag{4.20}$$

$$\overline{\varepsilon}_i = \frac{1}{V}\int_V \varepsilon_i(x_k)dV, \qquad i = 1,\ldots,6 \tag{4.21}$$

Where $\overline{\sigma}_i$, $\overline{\varepsilon}_i$ and V are the average stresses, average strains at the point x_k and volume of the RVE respectively.

4.2.6 Evaluation of volume averages

The Volume averages of the stresses and strains are evaluated using Eqs. (4.20) and (4.21), and these are implemented in finite element method as explained below:

$$\overline{\sigma}_i = \frac{1}{V}\int_V \sigma_i(x_k)dV = \frac{\sum_{t=1}^{n}(\sigma_i(x_k))_{m_t}(\Delta V)_{m_t} + \sum_{t=1}^{p}(\sigma_i(x_k))_{I_t}(\Delta V)_{I_t}}{\sum_{t=1}^{n}(\Delta V)_{m_t} + \sum_{t=1}^{p}(\Delta V)_{I_t}} \tag{4.22}$$

$$\overline{\varepsilon}_i = \frac{1}{V}\int_V \varepsilon_i(x_k)dV = \frac{\sum_{t=1}^{n}(\varepsilon_i(x_k))_{m_t}(\Delta V)_{m_t} + \sum_{t=1}^{p}(\varepsilon_i(x_k))_{I_t}(\Delta V)_{I_t}}{\sum_{t=1}^{n}(\Delta V)_{m_t} + \sum_{t=1}^{p}(\Delta V)_{I_t}} \tag{4.23}$$

where suffixes m_t, I_t represent the finite elements belonging to the matrix and the other phases reinforcing the matrix, respectively, and V represents the element volume in the finite element modelling, and the elemental stresses σ_i, strains ε_i can be obtained from the FE solution for each element of the RVE. These quantities are obtained at the centre of the each element (average of the quantities at the nodes which are attached to that element). For example, in order to calculate the average stress in the RVE, the elemental stresses corresponding to the inclusions (particles) and the matrix phases are captured and multiply the each element stress value with the corresponding element volume (this is obtained from the solution). Then add these quantities and divide the total value with the volume of the RVE. As an alternative approach, instead of using the field quantities at the centre of the element, one can choose the field quantities at the Gaussian points in the element (number of Gauss points in the element depends on their formulation) and can perform the averaging procedure. However, in the finite element model, if multiphase elements (different integration points of the elements are having different material properties) are used then it is more accurate to evaluate the averages using the quantities at the Gaussian integration points.

4.2.7 Evaluation of material elastic constants

Generally the linear behaviour of a material is described by 21 independent stiffness coefficients C_{ij}. This case corresponds to a material having no symmetry and such a material is called as triclinic material. As our material is considered as transversely isotropic, there exist ‘5’ independent constants for 3-Dimensional case and ‘3’ independent constants for 2-Dimensional case. The usage of this property leads to [53]:

$$C_{11} = C_{22} \qquad C_{13} = C_{23} \qquad C_{44} = C_{55} \qquad C_{66} = (C_{11} - C_{12})/2 \tag{4.24}$$

Thus invariance of the matrix for generalized Hooke’s Law [53], for transversely isotropic case, with 5 independent coefficients can be expressed in stiffness matrix form as:

$$\begin{bmatrix} \sigma_{11} \\ \sigma_{22} \\ \sigma_{33} \\ \sigma_{23} \\ \sigma_{31} \\ \sigma_{12} \end{bmatrix} = \begin{bmatrix} C_{11} & C_{12} & C_{13} & 0 & 0 & 0 \\ C_{12} & C_{11} & C_{13} & 0 & 0 & 0 \\ C_{13} & C_{13} & C_{33} & 0 & 0 & 0 \\ 0 & 0 & 0 & C_{44} & 0 & 0 \\ 0 & 0 & 0 & 0 & C_{44} & 0 \\ 0 & 0 & 0 & 0 & 0 & C_{66} \end{bmatrix} \begin{bmatrix} \varepsilon_{11} \\ \varepsilon_{22} \\ \varepsilon_{33} \\ \varepsilon_{23} \\ \varepsilon_{31} \\ \varepsilon_{12} \end{bmatrix} \tag{4.25}$$

For the simplification of plane stress condition, the stresses in the 3rd direction (i.e. z-direction) are considered to be negligible, hence $\sigma_{33} = \sigma_{23} = \sigma_{31} = 0$. So for the case of transversely isotropic composites for the plane stress, the generalized Hooke’s Law can be represented in stiffness matrix form as follows:

$$\begin{bmatrix}\sigma_{11}\\ \sigma_{22}\\ \sigma_{12}\end{bmatrix}=\begin{bmatrix}C_{11} & C_{12} & 0\\ C_{12} & C_{11} & 0\\ 0 & 0 & C_{66}\end{bmatrix}\begin{bmatrix}\varepsilon_{11}\\ \varepsilon_{22}\\ \varepsilon_{12}\end{bmatrix} \tag{4.26}$$

And in compliance matrix form as follows:

$$\begin{bmatrix}\varepsilon_{11}\\ \varepsilon_{22}\\ \varepsilon_{12}\end{bmatrix}=\begin{bmatrix}S_{11} & S_{12} & 0\\ S_{12} & S_{11} & 0\\ 0 & 0 & S_{66}\end{bmatrix}\begin{bmatrix}\sigma_{11}\\ \sigma_{22}\\ \sigma_{12}\end{bmatrix} \tag{4.27}$$

Evaluation of C_{11}, C_{12} and C_{66}

In our simulations mixed boundary conditions have been applied. The boundary conditions are applied in such a way that except the strains in the direction, in which effective coefficients have to be calculated, all other mechanical strains are zero. Unidirectional displacement is applied as a load. To determine C11 and C12 coefficients the boundary conditions are applied, as shown in the Fig. 4.3(a), to RVE in such a way that, edge A2 is constrained in all directions, edges A1, B1 and B2 are constrained in Y direction and unidirectional displacement (prescribed displacement), as a load, is applied on edge A1 in the positive X-direction. C_{11} and C_{12} can be evaluated as

$$\overline{\sigma}_{11}=C_{11}\overline{\varepsilon}_{11};\ C_{11}=\overline{\sigma}_{11}/\overline{\varepsilon}_{11} \tag{4.28}$$

$$\overline{\sigma}_{22}=C_{12}\overline{\varepsilon}_{11};\ C_{12}=\overline{\sigma}_{22}/\overline{\varepsilon}_{11} \tag{4.29}$$

For calculating C_{66} coefficient, the boundary conditions are applied, as shown in the Fig. 4.3(b). To avoid rigid body motion intersection point of the edges, A2 and B2, is constrained in all directions. Prescribed displacements are applied on the edges A1 and A2 along positive Y-axis and negative Y-axis respectively and on the edges B1 and B2 along positive X-axis and negative X-axis respectively. C_{66} can be determined as,

$$\overline{\sigma}_{12}=C_{66}\overline{\varepsilon}_{12};\ C_{66}=\overline{\sigma}_{12}/\overline{\varepsilon}_{12} \tag{4.30}$$

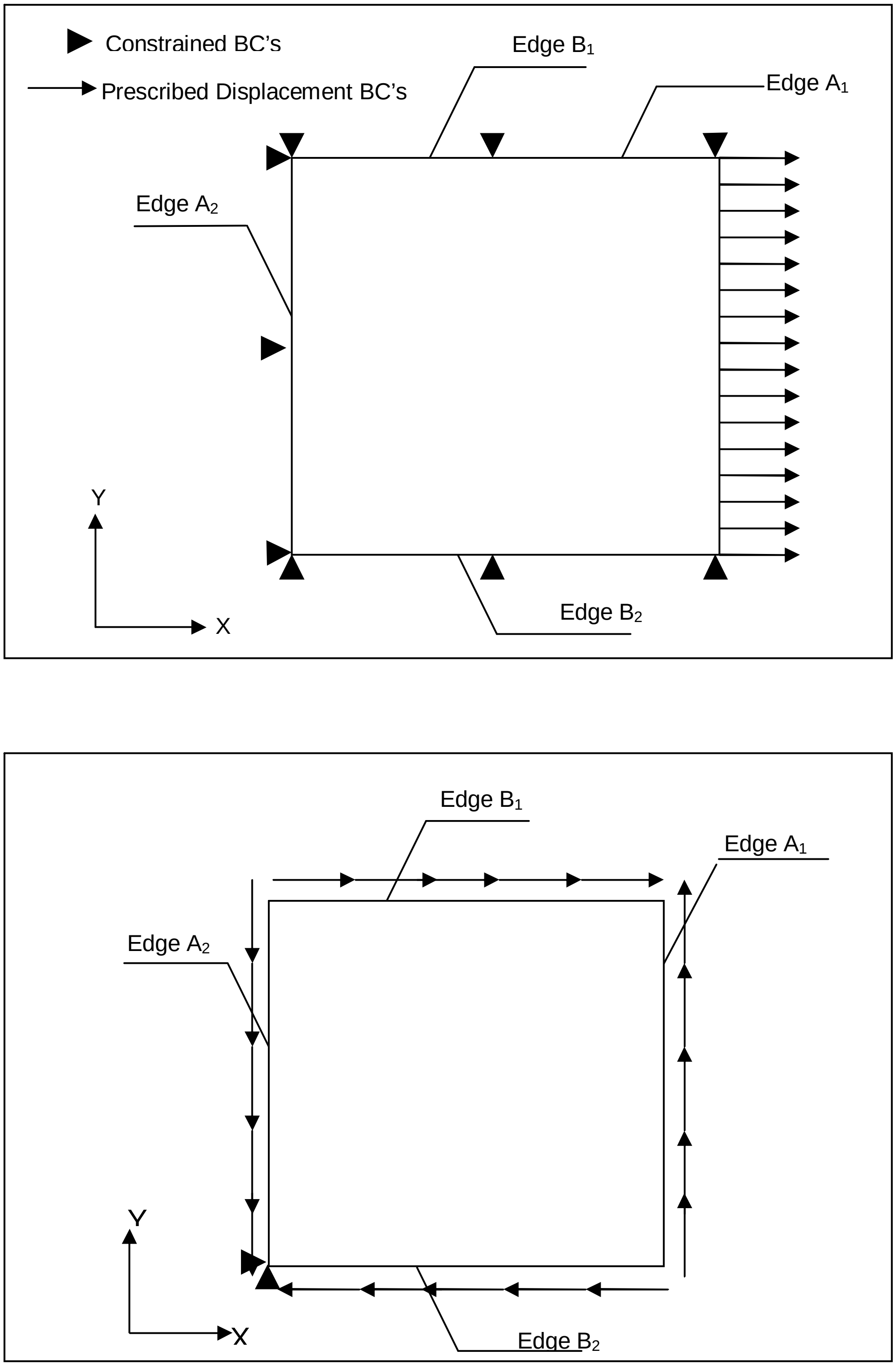

(a)

(b)

Fig. 4.3 Schematic diagram showing the application of mixed boundary conditions for the determination of stiffness coefficients (a) C11, C12 and (b) C66.

4.2.8 Evaluation of elastic moduli

The basic approach was followed in this thesis to evaluate the Elastic moduli of the effective material. By convention, the 3 elastic constants (for 2D) in transverse isotropic constitutive equations are the Young's modulus and Poisson's ratio in the *x*-*y* symmetry plane, E_{11} and v_{12} and the shear modulus in the *xy*-direction G_{12}.

The compliance matrix takes the form,

$$\begin{bmatrix} \varepsilon_{11} \\ \varepsilon_{22} \\ \varepsilon_{12} \end{bmatrix} = \begin{bmatrix} 1/E_{11} & -\upsilon_{12}/E_{11} & 0 \\ -\upsilon_{12}/E_{11} & 1/E_{11} & 0 \\ 0 & 0 & 1/G_{12} \end{bmatrix} \begin{bmatrix} \sigma_{11} \\ \sigma_{22} \\ \sigma_{12} \end{bmatrix} \tag{4.31}$$

Where

E_{11} = Transverse Young's modulus,

v_{12} = Transverse Poisson's ratio,

G_{12} = In plane shear modulus or Transverse Shear modulus

And by equating the corresponding elements of compliance matrix, obtained by inversing the stiffness matrix, to those of the compliance matrix of the form Eq. (4.31), the elastic moduli are evaluated.

$$C^{-1} = S = \begin{bmatrix} S_{11} & S_{12} & 0 \\ S_{12} & S_{11} & 0 \\ 0 & 0 & S_{66} \end{bmatrix} = \begin{bmatrix} 1/E_{11} & -\upsilon_{12}/E_{11} & 0 \\ -\upsilon_{12}/E_{11} & 1/E_{11} & 0 \\ 0 & 0 & 1/G_{12} \end{bmatrix} \tag{4.32}$$

So, from the above equation

$$S_{11} = 1/E_{11} \Rightarrow E_{11} = 1/S_{11} \tag{4.33}$$

$$S_{12} = -\upsilon_{12}/E_{11} \Rightarrow \upsilon_{12} = -S_{12} * E_{11} \tag{4.34}$$

$$S_{66} = 1/G_{12} \Rightarrow G_{12} = 1/S_{66} \tag{4.35}$$

The Shear modulus, G, of the material, which is defined as the ratio of shear stress to engineering shear strain on the loading plane, was evaluated using the following relation between Shear modulus, Young's modulus and Poisson's ratio [53].

$$G = \frac{E}{2(1+\upsilon)} \tag{4.36}$$

All the above calculations can be performed by applying the finite element analysis as explained in detail previously in this chapter.

Chapter 5

FEM Results of elastic properties and discussion

The overall behaviour of a composite material depends on the individual material properties of the constituents with which it is made of and many morphological parameters like grain size, volume fraction and arrangement of the reinforcement phase in the matrix. These latter required parameters may vary with different manufacturing routes.

Mo-Si-B alloys are studied for the influence of these parameters of intermetallics (Mo_3Si and T2 phases) and Molybdenum solid solution on the overall behaviour of the alloy. In this Chapter the influence of the volume fraction, the shape, the size and the arrangements of reinforcements on the effective material behaviour of various compositions of linear elastic Mo-Si-B alloy composites, using numerical homogenization techniques, is discussed. As the grains of all the phases in the microstructure are observed to be equiaxed, the results of 3-dimensional microstructure models are expected to be not much different from that of 2-dimensional microstructure modelling and hence we restricted ourselves to 2 dimensions in the modelling approach. The results, obtained using the finite element homogenization technique, are compared with different analytical methods and with experimental results available for a few different chemical compositions [55]. The experimental procedure for the determination of Elastic properties is discussed in detail in chapter 3.

5.1 Input properties

The material properties of the 3 constituents (Mo(ss), Mo_3Si and T2) of the composites are considered to be linear isotropic. The input material properties used for the 3 phases in simulation work for all compositions from RT to 1200°C are presented in Table 5.1. For Mo-0.5wt.%Si solid solution matrix (Mo(ss)), values were taken from the work done by Daniel et al, [20] who evaluated the elastic properties at different temperatures using the resonance method described in subsection 3.1.2.2, while for T2, Ihara et al. measured the polycrystalline isotropic elastic moduli in the Hill average from the elastic stiffness constants by the same method [56, 57]. For Mo_3Si, the RT properties were evaluated from the stiffness coefficients, C11 = 449GPa, C12 = 137GPa and C44 = 113GPa, obtained from the unpublished theoretical work of C. L. Fu [58]. As the elastic properties of T2 phase are observed to vary linearly with temperature, Mo_3Si phase is also assumed to behave in the same way and its input properties at higher temperatures were approximated accordingly with the available data. To the best of our knowledge it was the only available data for Mo_3Si.

Temperature [°C]	Young's modulus E [GPa]			Poisson's ratio		
	Mo(ss)	Mo_3Si	T2	Mo(ss)	Mo_3Si	T2
24°C	298	293	383	0.3	0.297	0.269
300°C	288	281	367	0.3	0.304	0.275
600°C	274	268	350	0.3	0.311	0.282
900°C	262	255	333	0.31	0.321	0.291
1200°C	247	242	316	0.32	0.329	0.298

Table 5.1: Input properties for different phases in the Mo-Si-B alloys used in FEM simulations.

5.2 Real microstructure simulations

Three real microstructures considered for the simulations are Mo-2.7Nb-8.9Si-7.7B, Mo-12Si-8.5B and Mo-12Si-10Nb-8.5B (all compositions are shown in at.%). The geometric models required for simulations from the real microstructures were prepared as explained in Chapter 4. The tensile loading conditions were implemented by applying mixed boundary conditions as explained in the previous chapter, in section 4.2.7. In case required, the microstructural features in the digital image, taken from SEM, were developed in such a way that they were suitable for modelling: i.e. if the individual phases in the microstructure are distinguishable only with the naked eye with their grey values, then individual phases are separated manually increasing their contrast such that they are suitable for PPM2OOF software to identify them and assign properties. The area fractions of phases in the microstructures were quantified using programming in an image analysis software product called IDL (Interactive Data Language) [41].

As the Mo-2.7Nb-8.9Si-7.7B alloy microstructure was taken after deformation at 1300°C and a strain rate of 10^{-4} s^{-1}, some voids had been formed, Fig. 5.1a(i). These voids were covered manually with respective phases compensating for the overall composition of the material. Mo solid solution, Mo_3Si and Mo_5SiB_2 appear light, medium- and dark-grey, respectively. For a clearer distinction between the phases Mo solid solution is assigned with white color in the model, Fig. 5.1a(ii). The volume fractions of the phases are quantified as Mo(ss) - 53%, Mo_3Si - 19% and Mo5SiB2 (T2) - 28%.

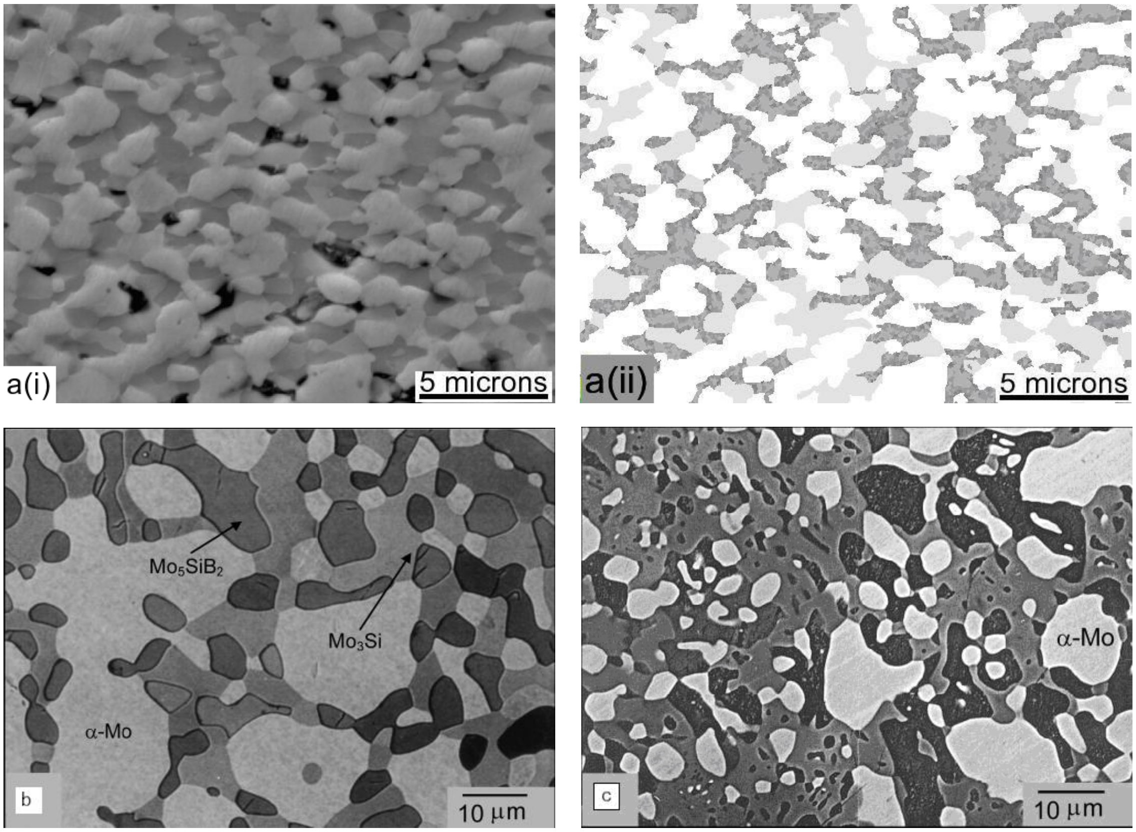

Fig. 5.1 Real microstructures used for simulations, (a) (i) SEM image taken from the gage section of Mo-2.7Nb-8.9Si-7.7B alloy after deformation at 1300°C and a strain rate of 10^{-4} s^{-1} and (ii) developed image of the same alloy, (b) Mo12Si8.5B and (c) Mo12Si10Nb8.5B alloys taken from [11, 38].

The mean grain sizes of all phases are around 1 μm and the microstructure can be considered as a triplex structure with a nearly continuous Mo(ss) matrix. It will be designated *microstructure 1* in what follows.

Young's modulus, Shear modulus, Bulk modulus and Poisson's ratio obtained from simulations are shown in Fig. 5.2. The Young's modulus is observed to decrease as expected as the temperature is increasing indicating the decrease in the stiffness of the material. Shear modulus and Bulk modulus show the same trend as the Young's modulus with the Bulk modulus decreasing slightly at higher temperature. On the other hand, Poisson's ratio shows increasing trend with higher temperatures. The elastic properties are in good agreement with the experimental results which will be discussed in the later section along with the comparison with analytical methods.

The elastic properties obtained from the FEM simulation for the alloy Mo-12Si-8.5B, which possesses a lower volume fraction of 38% of Mo(ss), which therefore can no longer be treated as a continuous matrix, Fig. 5.1b, are displayed in Fig. 5.3. Consequently, the volume fractions of the other phases amount to 27% and 35%, respectively, for Mo_3Si and T2 phase. The microstructure of this alloy will be numbered 2 in the following.

Finally, the third real *microstructure 3* used for our simulations was stemmed from the cast alloy Mo-12Si-10Nb-8.5B. In contrast to the former microstructures this material possesses a continuous network of the intermetallic phases Mo_3Si and T2, thus forming the matrix, with Mo(ss) islands distributed within this matrix, see Fig. 5.1c. The volume fractions of the three phases were quantified as Mo_3Si-29%, T2-35% and Mo(ss)-36%. The graphs showing the effective material properties, E, G, K and ν of the alloy evaluated from FEM simulations, are plotted in Fig. 5.4. The influence of microstructure on elastic properties is negligible due to not much difference in the elastic properties of the constituent phases.

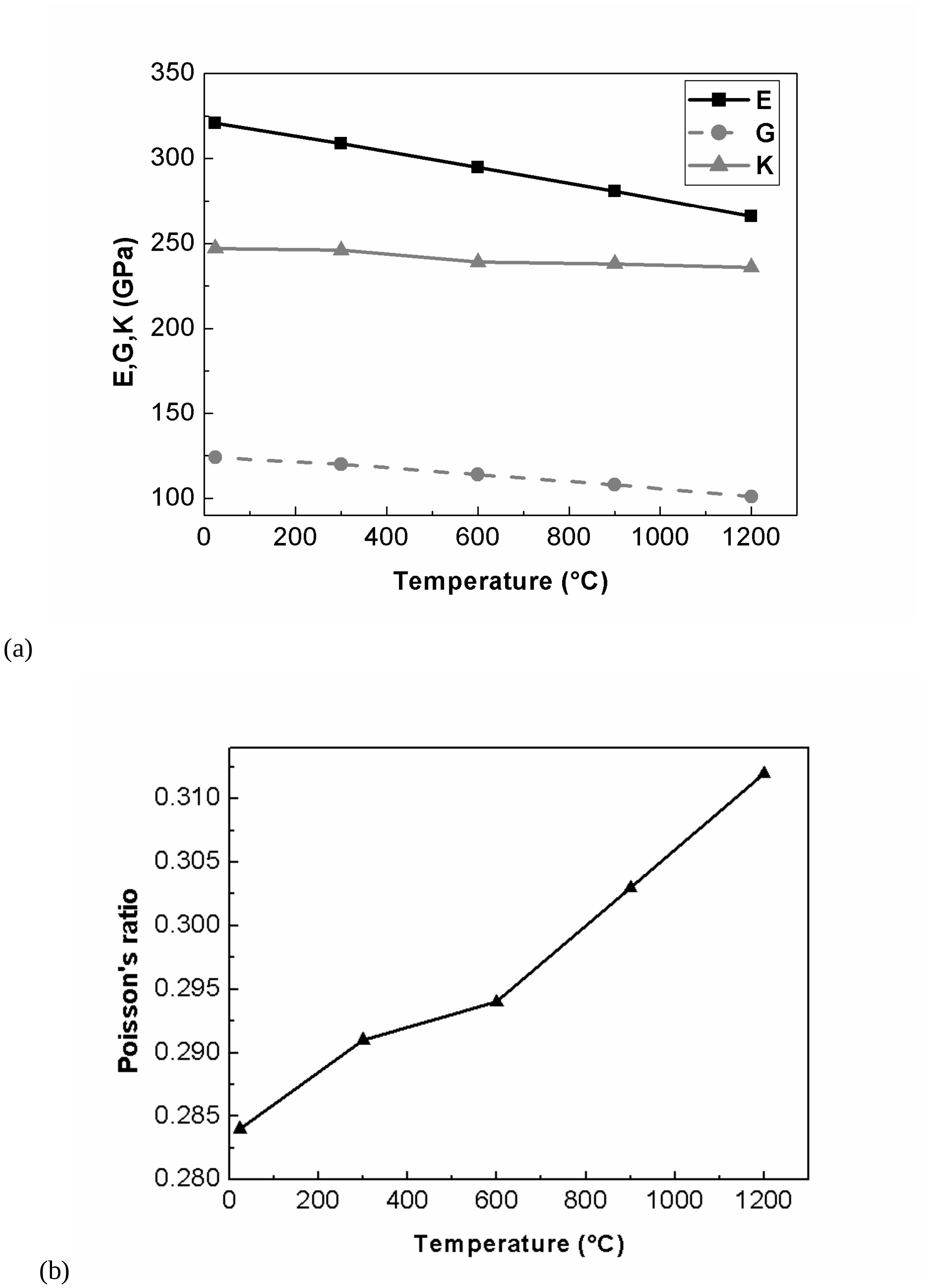

Fig. 5.2 Elastic material properties from FEM simulation of the alloy Mo-2.7Nb-8.9Si-7.7B between RT and 1200°C (a) Young's modulus, Shear modulus and Bulk modulus and (b) Poisson's ratio.

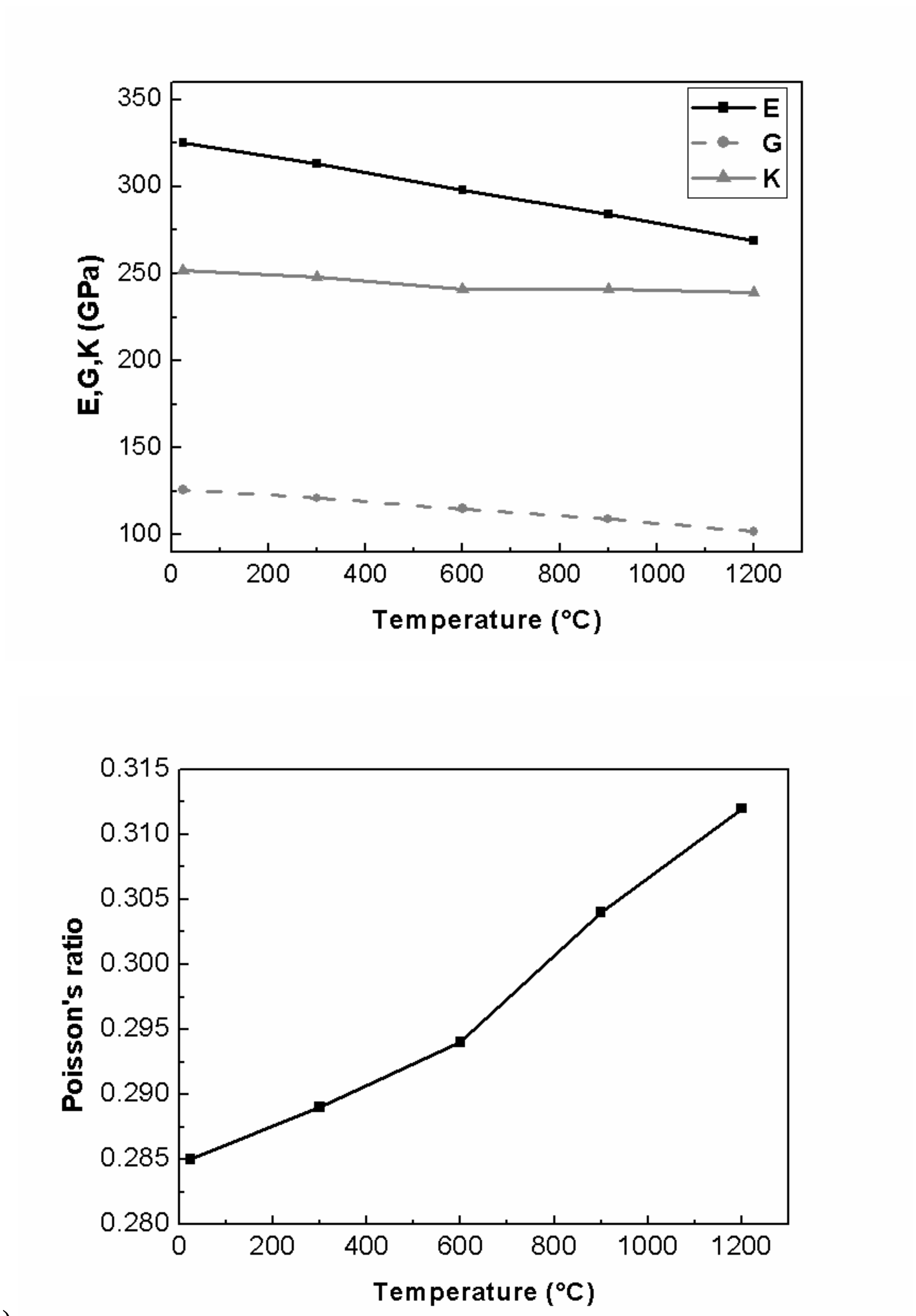

(a)

(b)

Fig. 5.3 Effective material properties from FEM simulation of the alloy Mo-12Si-8.5B between RT and 1200°C (a) Young’s modulus, Shear modulus and Bulk modulus and (b) Poisson’s ratio.

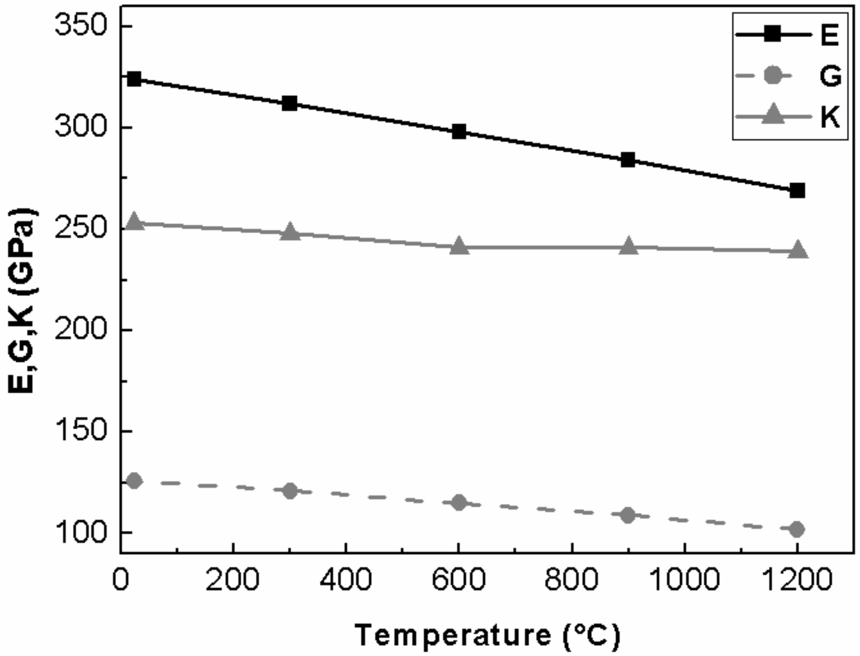

(a)

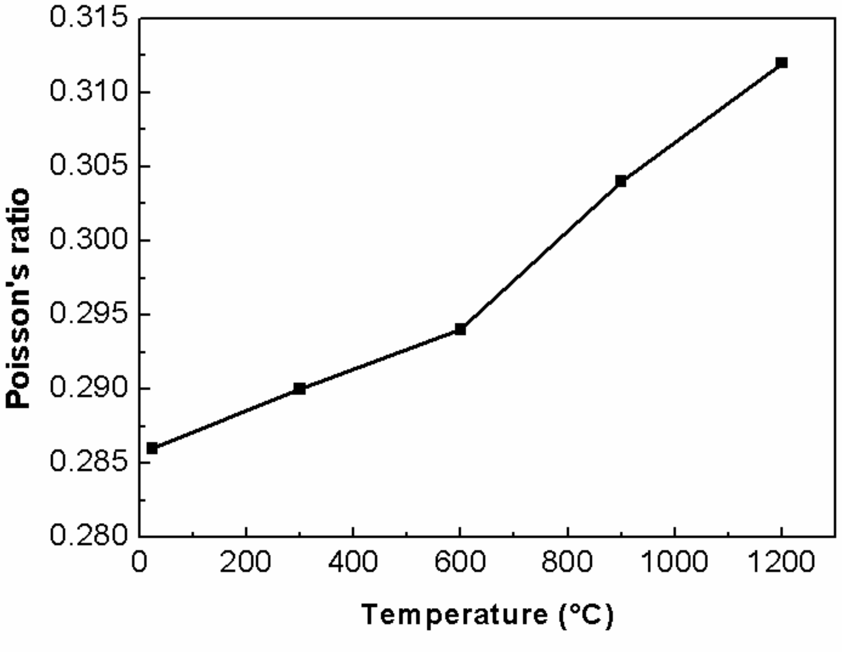

(b)

Fig. 5.4 Effective material properties from FEM simulation of the alloy Mo-12Si-10Nb-8.5B between RT and 1200°C (a) Young’s modulus, Shear modulus and Bulk modulus and (b) Poisson’s ratio.

5.3 Voronoi structure simulations

Two-dimensional Voronoi structures of different compositions have been generated as explained in the previous Chapter, in section 4.2.2 with the RVEs as representative volume elements. Generation of these RVEs took about 30 mins to 10 hrs depending on the number of Voronoi cells in the structures. The matrix Mo(ss) and the intermetallic phases Mo_3Si, T2, in the Voronoi structures, were assigned with white, light grey and dark grey colours, respectively, as shown in Fig. 5.5.

For each of seven different compositions, 55-15-30, 40-30-30, 30-35-35, 38-27-35, 20-40-40, 70-15-15 and 80-10-10 in the order of Mo(ss)%-Mo_3Si%-T2%, of Voronoi diagrams, representing Mo-Si-B alloys, five structures of varying fineness with 100, 500, 1000, 2000 and 3000 cells (grains) per unit area of 100x100 μm^2 in each structure have been produced. All the compositions were re-checked for volume fractions and adjusted manually after meshing, in few cases there was slight error due to different sizes of Voronoi cells and also due to meshing in the interfaces. The Voronoi structure representing the alloy Mo-2.7Nb-8.9Si-7.7B (microstructure 1) can be seen in Fig. 5.5, which was produced according to the quantified volume fractions of 53%, 19% and 28% of Mo(ss), Mo_3Si and T2 phases respectively.

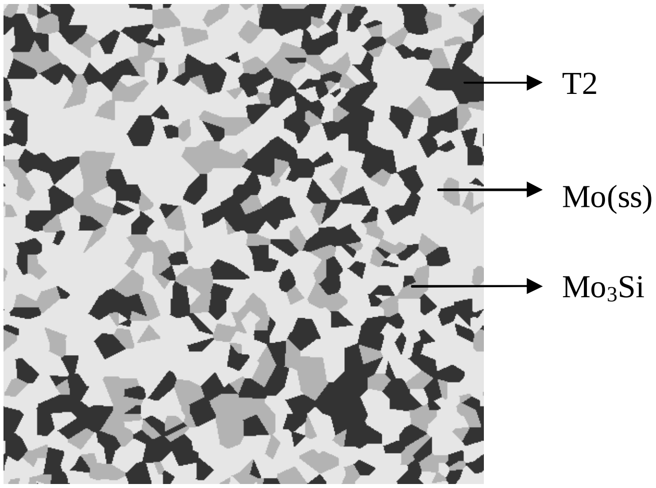

Fig. 5.5 RVE (comparable to microstructure 1) of composition 53%-19%-28% in the order of Mo(ss)-Mo_3Si-T2 generated from 1000 Voronoi cells.

5.3.1 Effect of grain size on elastic material properties

As mentioned above different Voronoi structures of varying coarseness were produced in order to study the effect of grain size i.e. coarseness of the structure on the elastic material properties. By varying the number of Voronoi cells in the structure, while maintaining constant size of square RVE of 100x100 μm^2, Voronoi structures of different fineness were generated. In our study RVEs with 100 cells and 3000 cells are the coarsest and the finest artificial microstructures, respectively. The simulation results, Young's modulus, shear modulus, bulk modulus and Poisson's ratio, were compared exemplarily for the composition 55-15-30 in the order of Mo(ss)%-Mo_3Si%-T2% for RVEs with 100, 500, 1000, 2000 and 3000 grains. Fig. 5.6 shows a negligible influence of the coarseness of the microstructure on the elastic material properties. Although slight variations can be observed in the effective material properties with a change in the size of the particles, these might be due to more number of particles inside the RVE by reducing its size for the same alloy composition.

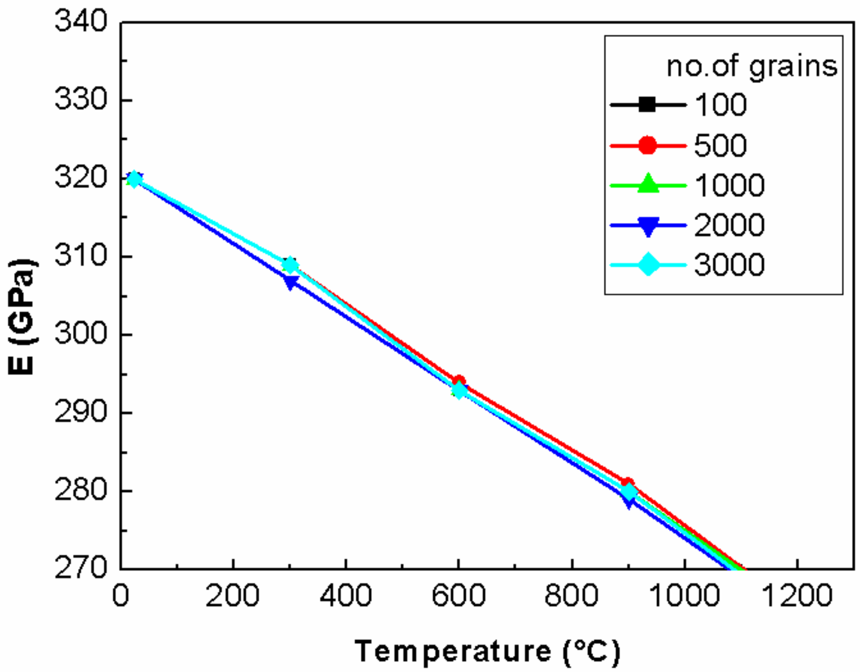

(a)

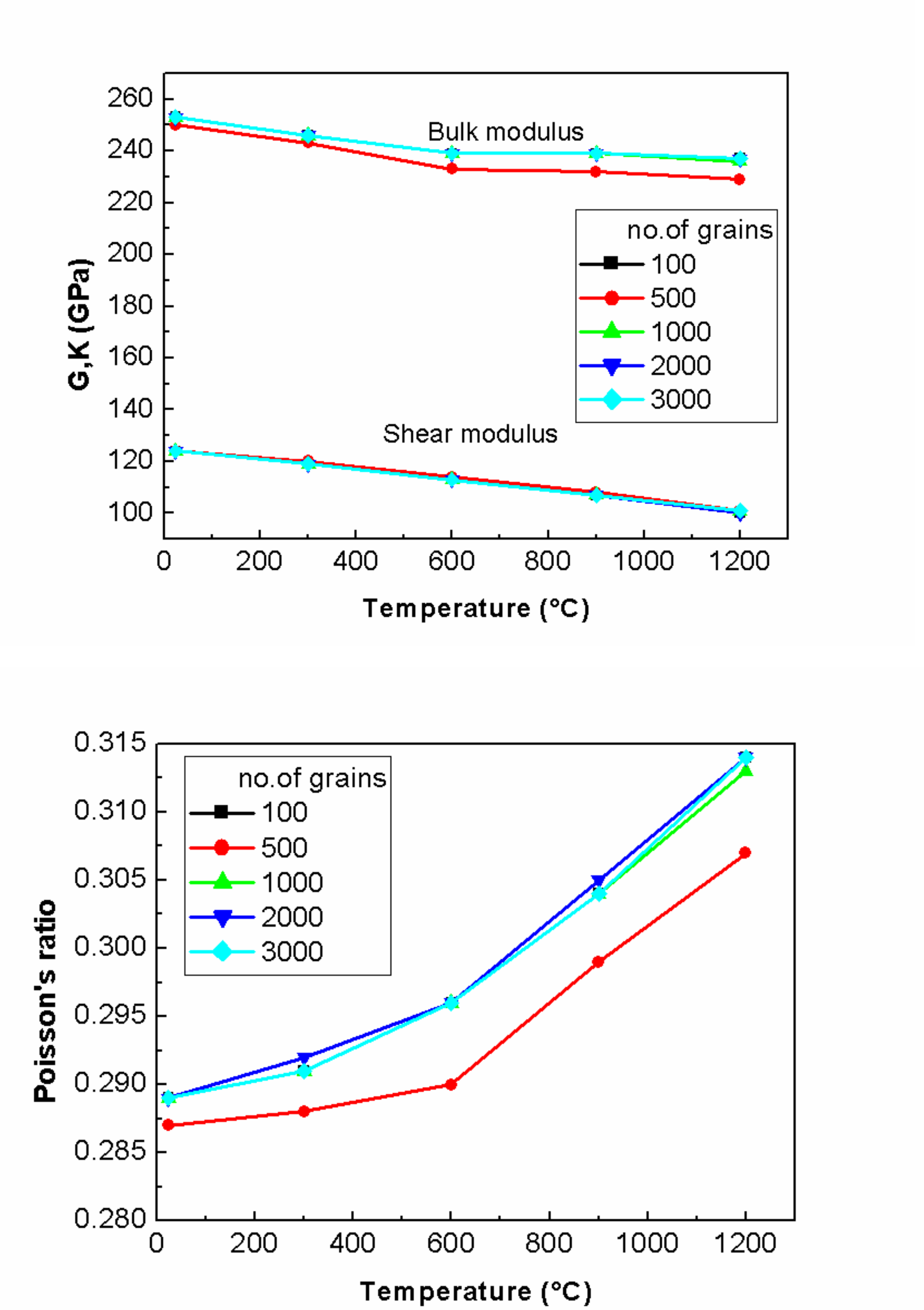

(b)

(c)

Fig. 5.6 Influence of coarseness of the microstructure of 55%Mo(ss)-15%Mo_3Si-30%T2 alloy on effective material properties at different temperatures a) Young's modulus, b) Shear modulus and Bulk modulus and c) Poisson's ratio.

5.3.2 Effect of volume fraction of different phases on elastic material properties

Keeping the ratio of volume fractions of the intermetallic phases Mo_3Si and T2 constant, Voronoi structures of compositions, varying from 20% Mo(ss) and 80% intermetallics to 80% Mo(ss) and 20% intermetallics, were produced and simulated at temperatures from RT to 1200°C to determine the influence of the volume fraction of molybdenum solid solution on the elastic material properties. As it can be seen in Fig. 5.7, increasing the volume fraction of Mo(ss) in the alloy decreases both, Young's modulus and shear modulus, whereas Poisson's ratio increases slightly at all temperatures. The zig-zag shape of Poisson's ratio curves, coming from small deviations in the values, can be attributed to the modelling approach used.

Alloy compositions in % (Mo(ss)-Mo_3Si-T2)	%Mo(ss)	E (GPa)	G (GPa)	K (GPa)	ν
20-40-40	20	**328**	**128**	**252**	**0.283**
30-35-35	30	**325**	**126**	**252**	**0.285**
40-30-30	40	**320**	**125**	**251**	**0.287**
50-25-25	50	**316**	**122**	**251**	**0.29**
60-20-20	60	**312**	**120**	**251**	**0.293**
70-15-15	70	**310**	**119**	**249**	**0.292**
80-10-10	80	**305**	**118**	**246**	**0.293**

Table 5.2: Effect of volume fraction of Mo(ss) on Effective material properties, Young's modulus (E), Shear modulus (G), Bulk modulus (K) and Poisson's ratio (ν) at RT.

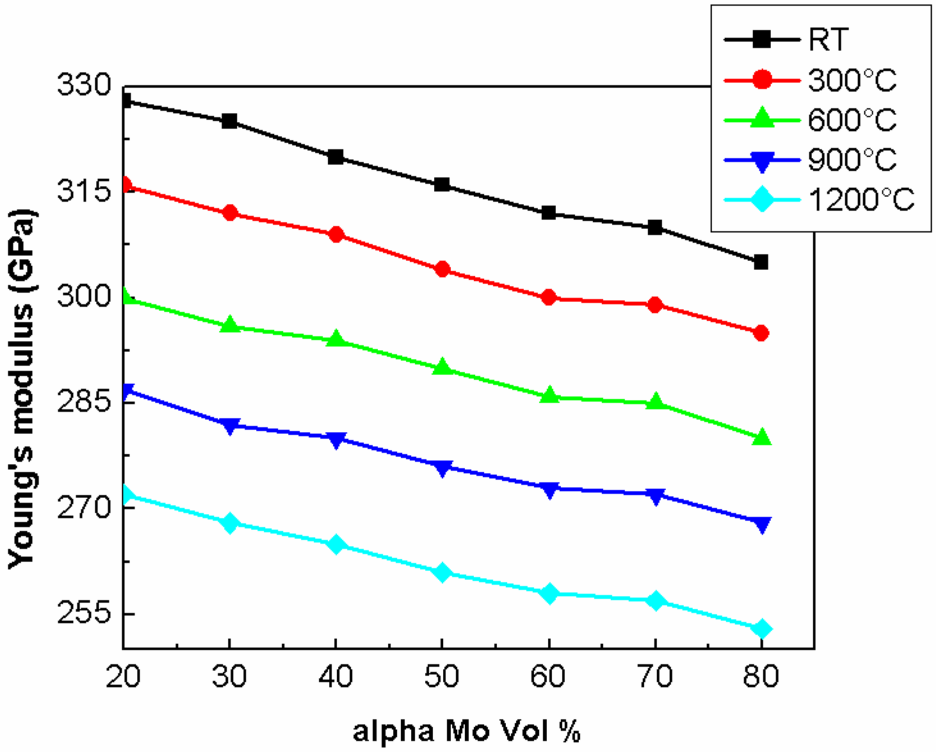
RT
300°C
600°C
900°C
1200°C
330
315
300
285
270
255
Young's modulus (GPa)
20
30
40
50
60
70
80
alpha Mo Vol %

(a)

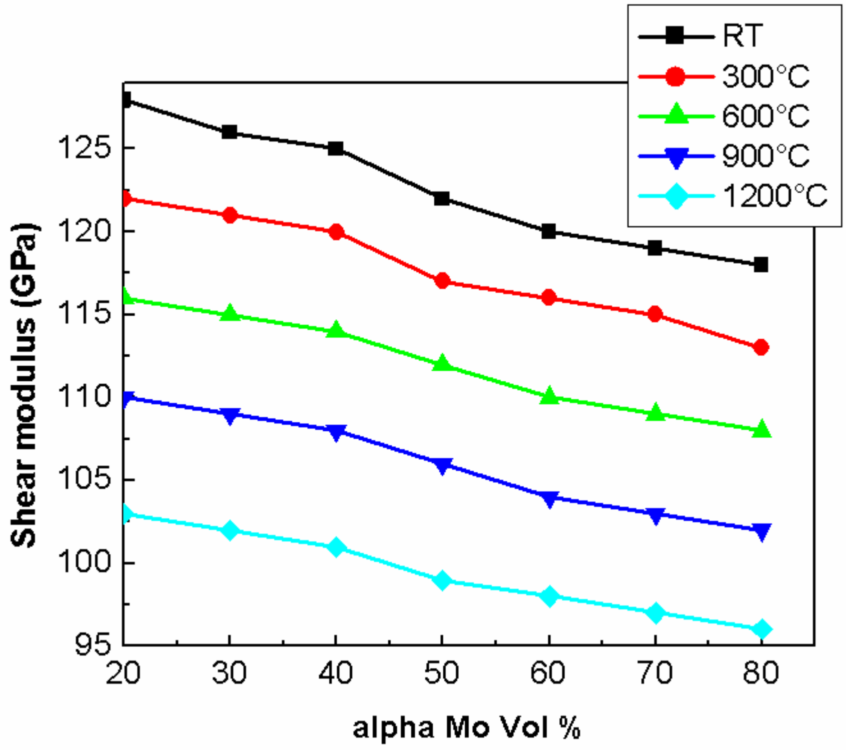
RT
300°C
600°C
900°C
1200°C
125
120
115
110
105
100
95
Shear modulus (GPa)
20
30
40
50
60
70
80
alpha Mo Vol %

(b)

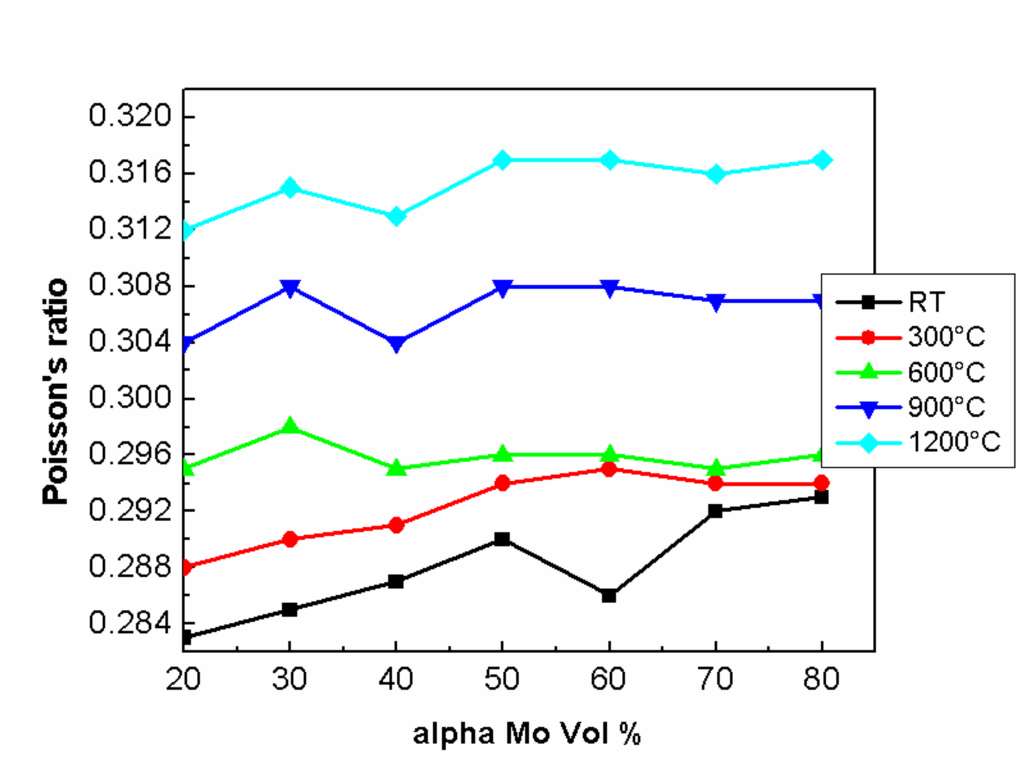

(c)

Fig. 5.7 Influence of volume fraction of Mo(ss) on effective material properties at temperatures between RT and 1200°C (a) Young's modulus, (b) Shear modulus and (c) Poisson's ratio.

5.3.3 Comparison of simulation results of Voronoi structures and real microstructures of similar composition

The Voronoi structure with the same composition, 53%-Mo(ss), 19%-Mo_3Si and 28%-T2, as that of real microstructure of the alloy Mo2.7Nb8.9Si7.7B was generated and simulated as explained in chapter 4, to determine E, G, K and ν. These properties were compared with that obtained from simulating the real microstructure of Mo2.7Nb8.9Si7.7B alloy. Fig. 5.8 shows that the effective properties obtained from Voronoi structures are, in essence, identical to that obtained from simulations of real microstructures indicating that Voronoi structures may represent the elastic behaviour of real microstructures in the case of homogeneous material.

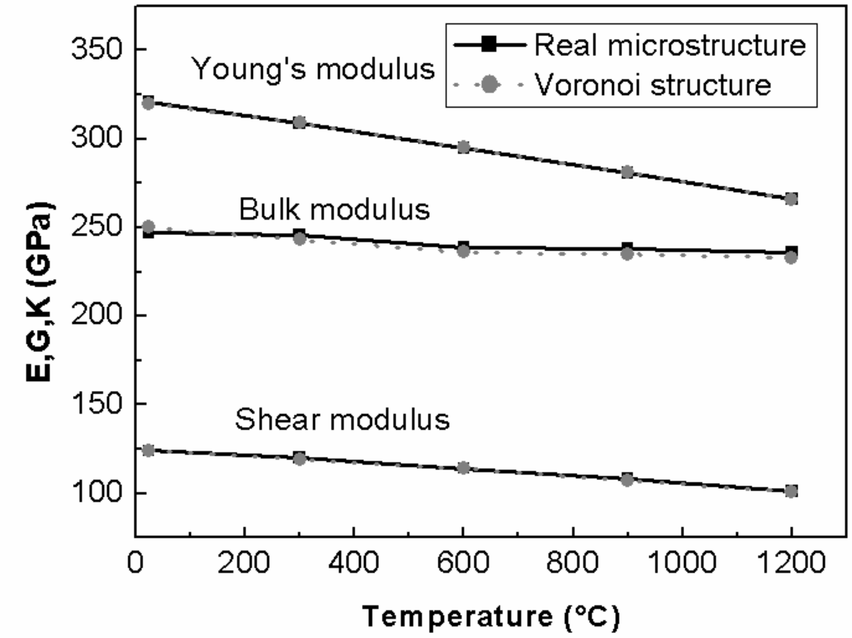

(a)

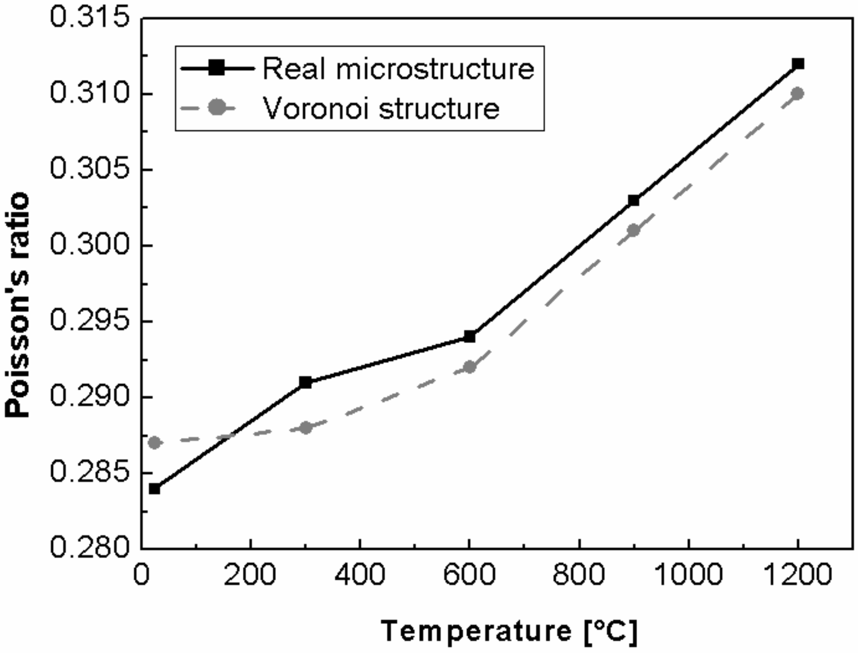

(b)

Fig. 5.8 Comparison of effective material properties deduced from FEM simulations of real microstructure of Mo2.7Nb8.9Si7.7B alloy and Voronoi structure representing Mo2.7Nb8.9Si7.7B alloy.

5.4 Comparison of FEM results with experimental results and analytical methods from the literature

Young's modulus (E), Shear modulus (G), Bulk modulus (K) and poison's ratio (ν) which were evaluated for real microstructures and Voronoi structures of different compositions as shown above, were finally compared with the experimental results and, some well-known analytical methods. Fig. 5.9 shows the comparison for the Mo2.7Nb8.9Si7.7B alloy at different temperatures. Young's modulus and shear modulus obtained by numerical homogenization technique are between Voigt and Reuss bounds as the upper and lower limit, respectively [42, 43], and are closest to the Hashin-Shtrikman approach [44, 45] with an error of less than 0.6%. In case of the Bulk modulus and of Poisson's ratio the maximum error is less than 3.5% and 1%, respectively. The error between FEM simulations and experiments is less than 2% for Young's modulus, 2.6% for shear modulus, 1.7% for bulk modulus and 1% for Poisson's ratio, respectively. Bulk modulus and Poisson's ratios obtained from FEM simulations are much closer to the experimental results than that from analytical methods, which can be due to the fact that Bulk modulus is very sensitive. Evidently all simulation results are in between Voigt and Reuss bounds as expected.

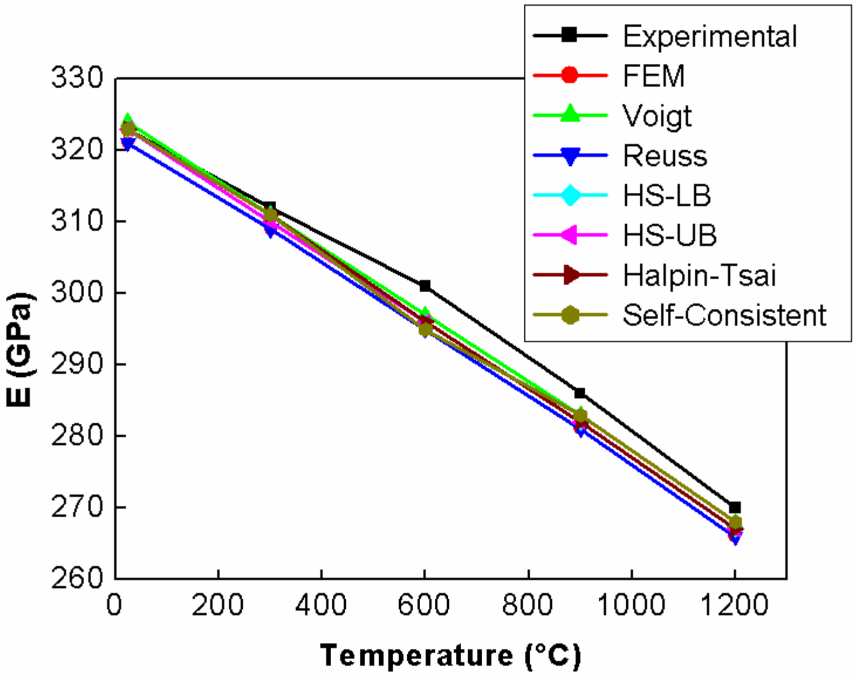

(a)

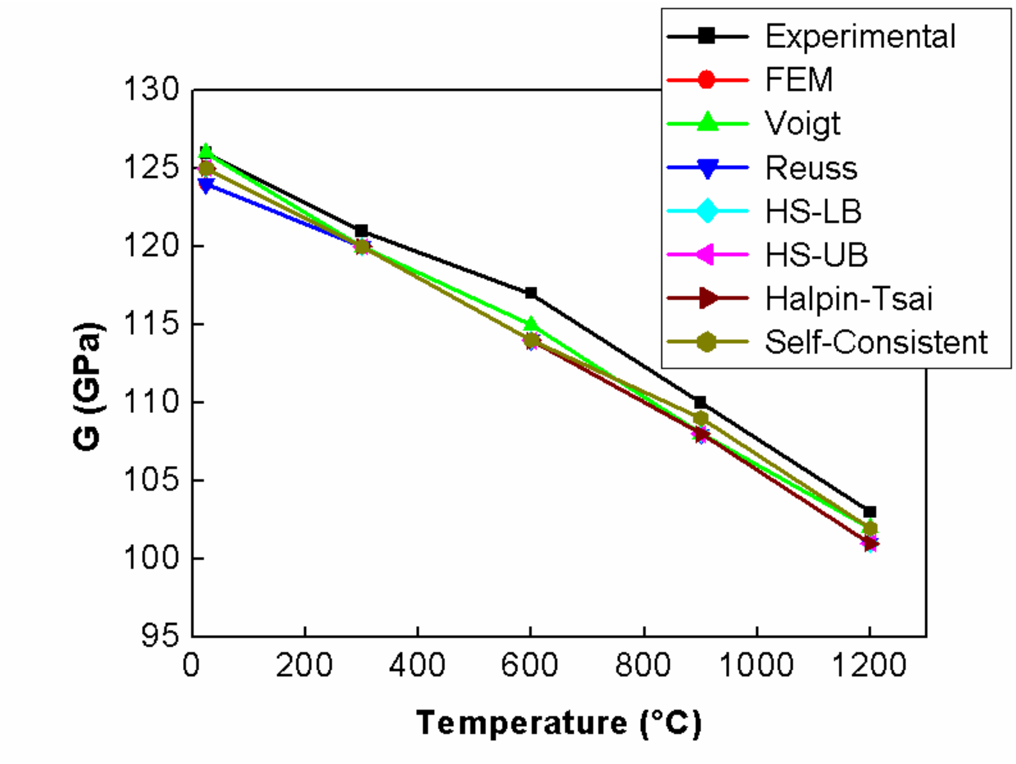
Experimental
FEM
Voigt
Reuss
HS-LB
HS-UB
Halpin-Tsai
Self-Consistent
130
125
120
115
110
105
100
95
G (GPa)
0
200
400
600
800
1000
1200
Temperature (°C)

(b)

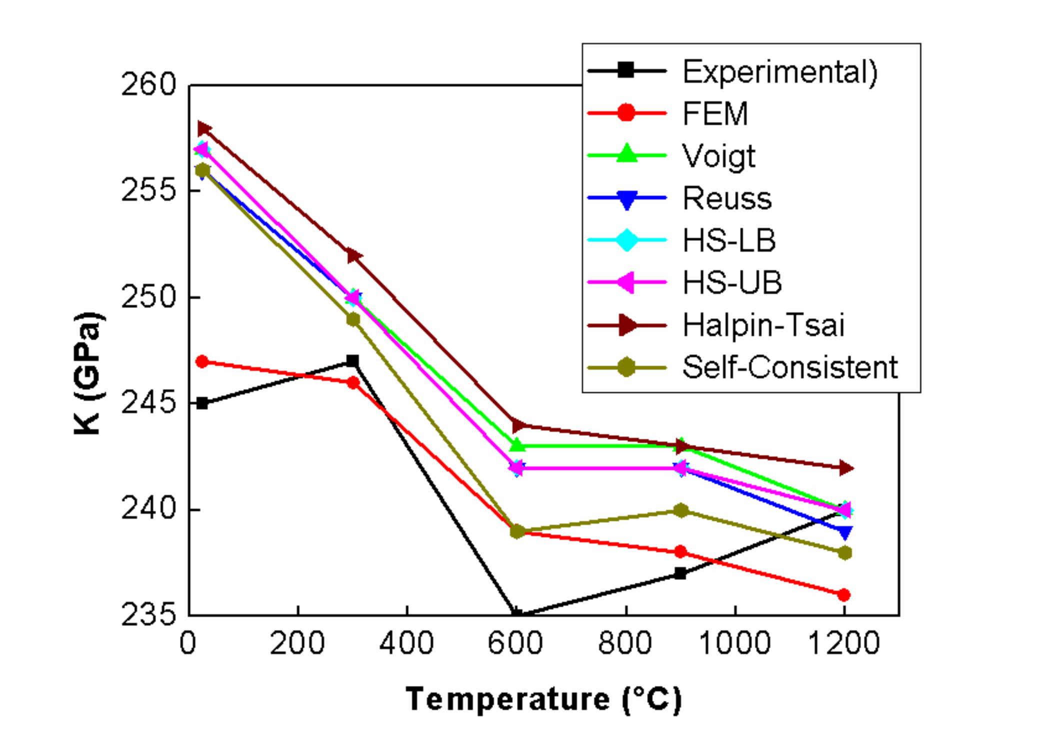
Experimental)
FEM
Voigt
Reuss
HS-LB
HS-UB
Halpin-Tsai
Self-Consistent
260
255
250
245
240
235
K (GPa)
0
200
400
600
800
1000
1200
Temperature (°C)

(c)

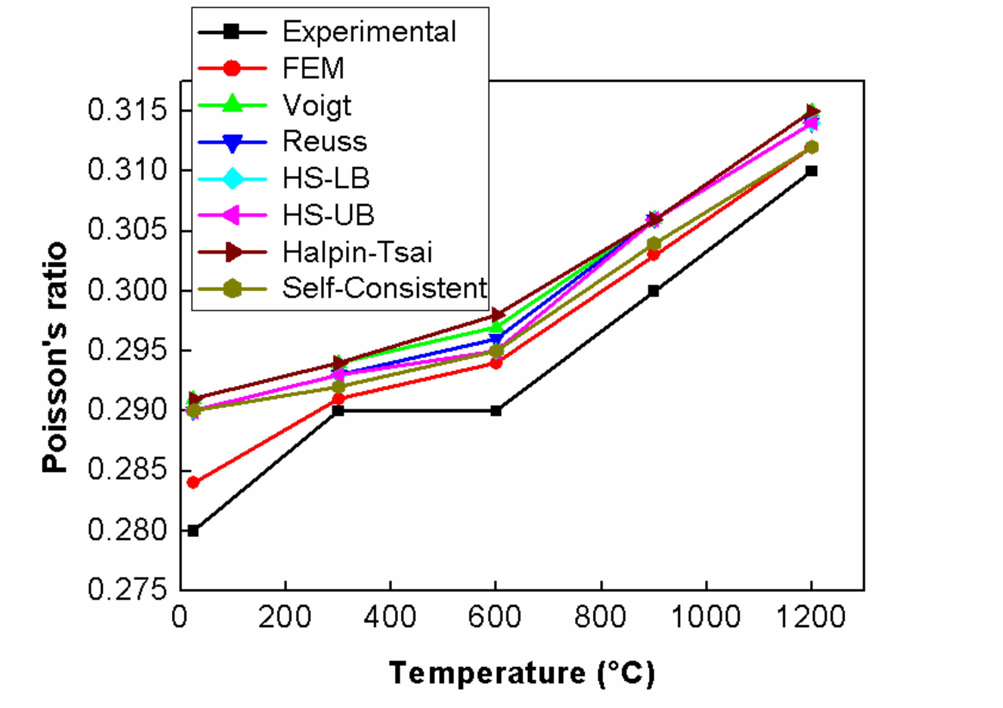

(d)

Fig. 5.9 Comparison of effective material properties of Mo2.7Nb8.9Si7.7B alloy with experimental and other analytical methods (a) Young's modulus, (b) Shear modulus, (c) Bulk modulus and (d) Poisson's ratio.

5.5 Case study

We did a case study with the parametric estimation, varying the input properties, and changing the arrangement of intermetallics in two simple ways to observe how the properties vary with the change in arrangements if the difference between the properties of the matrix and the reinforcing phase (intermetallics) were large. And also the comparison of simulated results was made with the Analytical methods in the case of the two arrangements.

5.5.1 Phase arrangements

Two RVEs of the same dimensions 100x100 μm^2 were generated with two types of arrangements of intermetallics, with a volume fraction of 30%, in the Mo(ss) matrix. In the model 1, the Intermetallics are distributed more like clusters as shown in Fig. 5.10(a), where as in model 2 they are distributed uniformly in the matrix with almost constant distance between the particles (Fig. 5.10(b)).

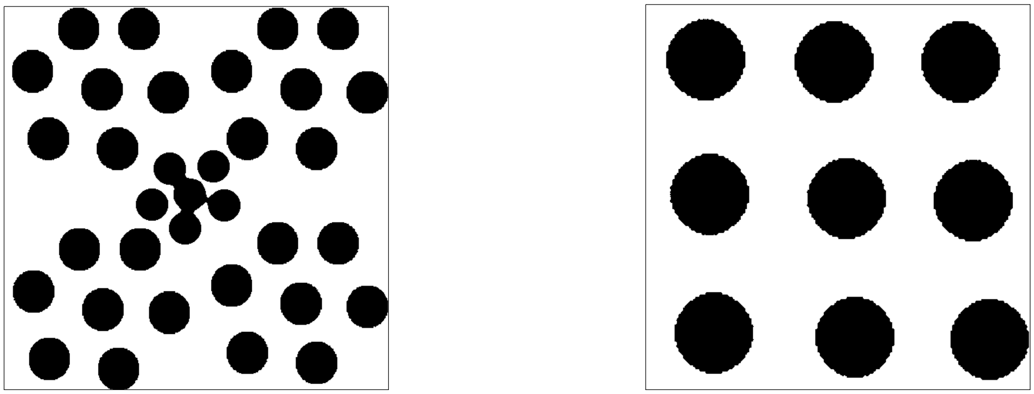

(a) (b)

Fig. 5.10 RVE models, with 30% volume fraction of intermetallics, considered for case study (a) model 1 and (b) model 2.

5.5.2 Parametric Estimation

For the 2 models, two sets of input properties were used as shown in Table 5.3. In the first case the original properties for both phases were used and in the second case the input properties were increased so that the difference between the input properties of matrix and intermetallic phases is large. In the first case the common input properties for both the intermetallics Mo_3Si and T2 phase were evaluated using the rule of mixture and were considered as a single phase. In the second case a random input value was taken for the intermetallics phase as given in Table 5.3.

Input properties	**case-1**		**case-2**	
	matrix	intermetallics	matrix	intermetallics
E (GPa)	298	338	1000	200
ν	0.30	0.283	0.30	0.25

Table 5.3: Input properties used in two different cases of case study.

5.5.3 Comparison of FEM results with Analytical methods

As it is evident from the results, shown in Table 5.4, the FEM gives different results depending upon the arrangement of the phases, while the analytical methods show the same results for both cases, proving that these analytical methods do not reflect the elastic behaviour of real microstructures. And also as the difference between the elastic properties of the phases in the material is more, the Analytical bounds are very wide-spread.

Effective Properties	Model 1 FEM	Model 2 FEM	Voigt	Reuss	HS-UB	HS-LB	Halpin-Tsai	Self-Consistent
E (GPa)	588	634	760	455	666	550	705	634
G (GPa)	227	215	293	179	260	217	258	250
K (GPa)	460	448	624	325	503	395	874	458
v	0.287	0.264	0.297	0.267	0.279	0.268	0.366	0.269

Table 5.4: Comparison between the effective properties obtained from FEM and Analytical methods for model 1 and model 2 for case-2.

Effective Properties	Model 1 FEM	Model 2 FEM	Voigt	Reuss	HS-UB	HS-LB	Halpin-Tsai	Self-Consistent
E (GPa)	309	309	310	309	310	310	310	310
G (GPa)	119	119	120	119	120	120	120	120
K (GPa)	250	250	252	252	252	252	253	252
v	0.294	0.294	0.295	0.295	0.295	0.295	0.296	0.294

Table 5.5: Comparison between the effective properties obtained from FEM and Analytical methods for model 1 and model 2 for case-1.

On the other hand with the original input parameters (see Table 5.3), the analytical bounds are narrow as the difference between the real properties of the matrix and that of the intermetallics is not very pronounced. Thus, the comparison of the results for case-1 in table 5.5 shows that all methods yield the same results irrespective of the arrangement of the different phases. To conclude, in the both the cases the FEM results are bounded by the Voigt and Reuss approach, respectively, yielding that the approach and the model chosen produce physically correct values.

Chapter 6

Damage Analysis

The demand for materials for elevated temperature applications in the aerospace industry beyond the capability of Ni-base superalloys has generated significant research interest in refractory metals and their alloys, intermetallics and ceramics. Thus, multiphase Nb-based alloys and Mo-based alloys have been the focus of research attention over the past few years. Mo-based alloys represent a higher-temperature alternative but suffer from oxidation problems. In this regard, molybdenum silicides and borosilicides have shown promise in improving the oxidation and creep resistance [59-60], leading to the development of two specific Mo–Si–B alloy systems by Akinc and coworkers [26, 59-61] and Berczik [62-63]. However, the silicide composites are brittle and provide little fracture resistance for most structural applications without significant additional toughening. Clearly, the strength and toughness properties of the alloys depend on the volume fraction of the ductile Mo(ss) phase and the scale of the microstructure. Recent studies on the microstructure and properties of single- and multiphase alloys in the Mo–Si–B system, evaluating different processing routes can be found in [11, 38, 64 and 65]. The objective of this work is to numerically analyze the effect of volume fraction and grain sizes of different phases in the Mo-Si-B alloys on their damage behaviour, tensile strength and resistance to crack growth.

Various microstructures are tested numerically under the same loading conditions. In our approach the microstructure simulations are performed based on Voronoi tessellation in which the surface is discretized into polygonal cells and each polygon is assumed as a single grain. Four real microstructures were quantified and Voronoi structures of the same compositions were generated and simulated using finite element analysis for their damage behaviour, tensile strength and plastic failure strains. Several three-phase and two-phase alloy compositions of Voronoi structures representing Mo-Si-B alloys were generated to investigate the influence of various parameters such as volume fraction and the grain size of individual phases.

In the present work Element Elimination Technique (EET) [65, 66] is used, which allows the simulation of crack initiation and growth without any additional assumptions about the crack path. The procedure and steps involved in implementation of simulation of damage behaviour using EET in ANSYS are explained in the following.

6.1 Element Elimination Technique (EET)

The problem considered in this research work requires an approach which allows to model both fracture and damage evolution using the same criteria, and to take into account the microstructure of the material without prescribing a crack path. In order to solve this type of problem, Wulf [67] applied the Element Elimination Technique (EET), which, by the author's opinion, has all advantages of the numerical methods, used for simulation of crack growth, such as Cohesive Zone models (CZM), Computational cell methodology (CCM), Cohesive Surface model (CSM), embedded crack model (ECM) etc. Comparing EET and CZM, it can be noted that the weak point in the CZM [68] is the requirement of the crack path prescribing. Therefore, neither crack deflection, nor variations of crack path (which may lead to sufficient variations of fracture energy [69]) can be described in the framework of the CZM satisfactorily. Other advantages of EET are that both micro-damage and crack propagation can be simulated using the same local damage criteria.

Numerically, the element elimination can be realized in two ways: by element softening and by element removal [65, 66, 70]. Element 'softening' is done if each element is assumed to be weakened as the local stress or damage parameter exceeds a critical level. The Young's modulus of the elements to be softened is set 1. . .2 orders of magnitude lower than that of the initial material. Another way is to remove the elements from the model, and then to restart the simulation without the eliminated elements, using the RESTART option in ANSYS. In this research work, the element elimination technique (EET) used is based on the removal of finite elements, which satisfy some failure condition (which is to be defined for each material to be considered). In such a way the formation, growth and coalescence of voids or micro-cracks, and the crack growth are simulated. As criteria of local failure, both global (external loads or displacements) and local (i.e. defined for a given element; for instance, plastic strain, von Mises stress, hydrostatic stress, etc.) values as well as any combination of these values can be used. Besides, EET can be used both for multiphase and single phase materials (in doing so, the criteria of element elimination should be chosen separately for each phase of multiphase material). In this work EET for single phase material is implemented comparing the major principal stresses of the elements with their critical stresses.

To eliminate an element, all components of stress tensors in this element are set to zero. As a result, all forces in this element become zero as well, and therefore, this element stops to transmit load to neighboring non-eliminated elements. The element elimination does not mean that an eliminated element is really removed from the FE mesh, yet, it stops to interact with neighboring elements. In solving the problem the stiffness matrix has to be corrected after the element elimination. This is done by setting the Young's modulus of the eliminated elements equal to zero. In order to avoid numerical problems related to strong local loss of equilibrium, the stresses are set to be equal to zero in several steps (called 'relaxation steps'). The Young's moduli in the eliminated elements are set to be equal to zero in the last relaxation step. The main advantages of this approach are that both micro-damage and crack propagation can be simulated although some mesh dependence is to be expected.

6.2 Mechanical properties of the constituents of Mo-Si-B alloys

For the numerical simulation of damage behaviour, the required mechanical properties of the constituents were taken as: for Mo(ss), Young's modulus – 298 GPa and Poisson's ratio – 0.30 [20]; for Mo_3Si, Young's modulus – 293 GPa and Poisson's ratio – 0.297 [58]; for T2, Young's modulus – 383 GPa and Poisson's ratio – 0.269 [56, 57].

The individual grains in each phase were assigned different failure stresses, evaluated from the respective fracture toughness of each phase where the critical crack length is set equal to their grain sizes by using the relation (6.1).

$$K_I = \sigma_{YS} \sqrt{\pi \, a_{cr}} \tag{6.1}$$

Where

K_I = Fracture toughness of the constituent phases

σ_{YS} = tensile stress

a_{cr} = critical crack length = grain size

Fracture toughness values for the three phases were taken from literature: for the Molybdenum solid solution - 7 MPa√m [20] for Mo_3Si - 3 MPa√m [71] and for T2 - 2 MPa√m [56]

6.3 Procedure for model generation and simulation of damage behaviour

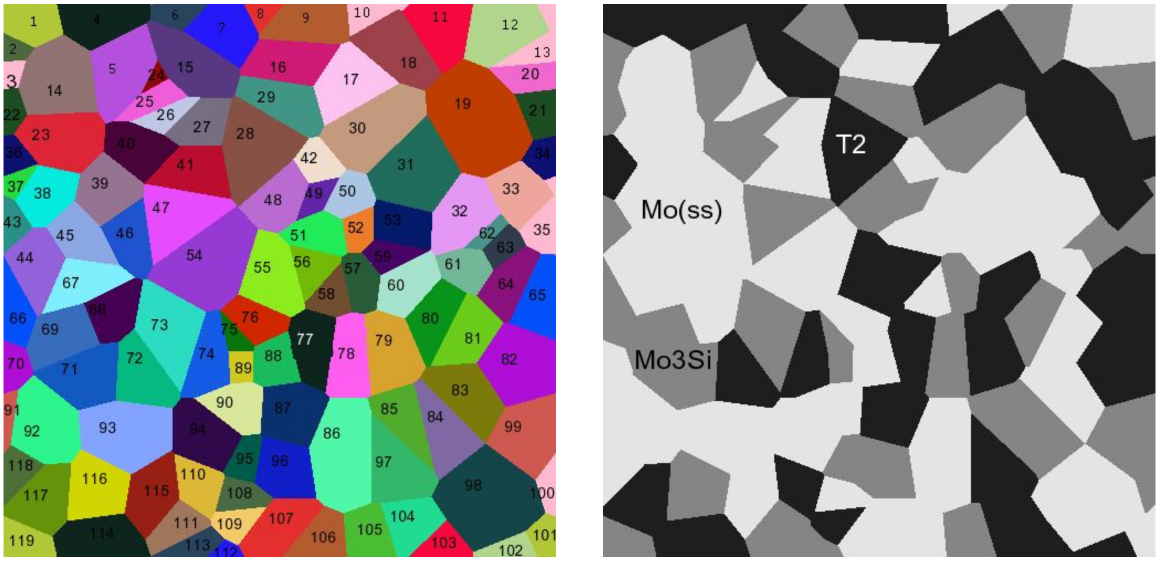

(a) (b)

Fig. 6.1 (a) Voronoi cells, each numbered cell representing a grain and (b) material model, after the grains were categorized in to different phases.

In this approach the microstructure simulations were performed based on Voronoi tessellation in which the surface was discretized into polygonal cells and each polygon was assumed as a single grain. For simplicity all the Voronoi cells were numbered, which represent the grains of different phases in the microstructure, as shown in fig. 6.1. The numbers were picked manually to categorize into the respective phases, adjusting their volume fractions, to achieve eventually the composition of interest. The average grain size of individual phases was calculated, from the measured individual grain sizes using IDL [41] and image J [72]. The geometric model was created in PPM2OOF as explained in Chapter 4 and data set representing the finite element model was exported into ANSYS where simulation was performed. The two-dimensional simulations were performed using six-node plane2, plane stress elements. In our approach the interfacial zone between aggregates and the matrix was disregarded and rigid bond was assumed. Linear elastic isotropic material behaviour was assumed for all the phases and also the damage behaviour was restricted to tensile failure. Mixed boundary conditions were applied as explained in the Chapter 4 to simulate tensile loading conditions. Unidirectional incremental displacements were applied as load in subsequent steps until the material failed completely. To do this manually is an extensive process, so a user defined FORTRAN program was developed to apply the load steps in batch mode, checking for the eliminated elements after each load step and resetting all components of stress tensors in those elements to zero and to apply the next load subsequently. As all forces in the eliminated elements become zero as well, therefore, this element stops to transmit load to neighboring non-eliminated elements. The load convergence test was made to determine the incremental load to be applied in simulation.

The alloy compositions, for which Voronoi models were generated and used in the simulation of damage behaviour, are shown in table 6.1 along with the volume fractions of the phases present.

Alloy Compositions	Volume fractions of phases (%)		
	Mo(ss)	Mo_3Si	Mo_5SiB_2 (T2)
Mo-13Si-12B	25	20	55
Mo-9Si-8B	55	15	30
Mo-6Si-5B	67	11	22
Mo-6Si-8B	67	-	33

Table 6.1: Alloy compositions used for damage simulation and volume fraction of the phases present.

For each Voronoi composition five different approaches with grain sizes 1µm, 3µm, 5µm, 7µm and 9µm were considered.

6.4 Load increment Convergence Test

The numerical investigations were made in order to study the influence of the load increments applied for simulations of damage behaviour. For 55-15-30 composition (in the order of Mo(ss)-Mo_3Si-T2) of 100x100 µm^2 RVE size, different load increments (load is applied in terms of displacement) have been applied in each case, starting from 0.005µm and decreasing it in each step until the stress to failure converged for at least 3 continuous load increment values. The error in tensile strength at 0.004µm load increment is around 2.3% but it gradually decreased as the load increment is reduced further and it converged at 0.0004µm, see fig. 6.2. In what follows 0.0004µm load increment was used in all our damage simulations.

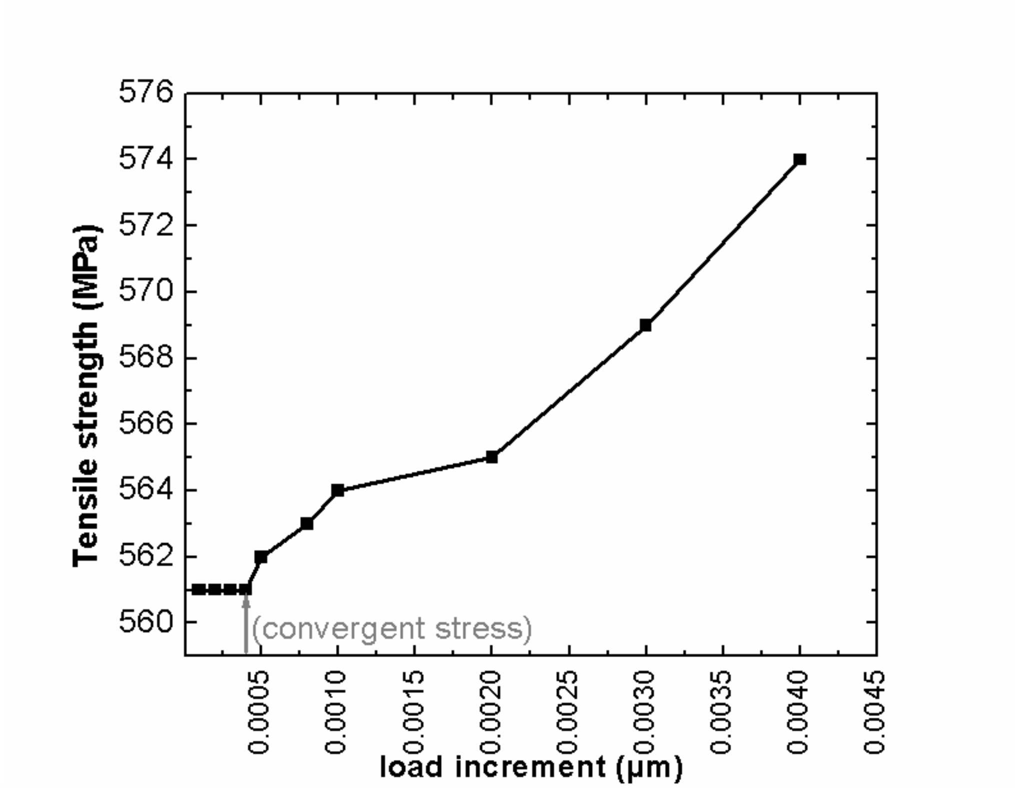

Fig. 6.2 Convergence study of load increment: Tensile strength to failure reduces with decreasing load increment for a RVE of 100µm edge length.

6.5 Finite element simulation of Voronoi structures of various alloy compositions for their damage behaviour

6.5.1 Comparison of tensile strengths

The alloy compositions as shown in Table 6.1 were quantified for the volume fractions of the phases present, Voronoi structures of similar compositions were produced as explained in Chapter 3, and simulations were carried out for 2D plane stress conditions for assessing their damage behaviour. For all the simulations performed, the tensile strengths and plastic failure strains from stress-strain curves were determined numerically. Figure 6.3(a) shows the stress-strain curves for the simulated Voronoi structures of the alloy compositions with an average grain size of 1µm. The far-field applied strain at the beginning of crack growth at which many particles fail and the falling branch of the stress-strain curve begins will be called ‘‘initial failure strain’’ and the final applied strain at which the material fails completely will be designated as “plastic failure strain” hereafter. Figure 6.3(b) shows the comparison of plastic failure strains of the simulated compositions for various grain sizes. The Voronoi composition of the alloy Mo-6Si-5B, which has 67% Mo(ss), has the highest tensile strength while Mo-9Si-8B has the highest plastic failure strain compared to that of the other compositions, offering more resistance for the complete failure of the material. By contrast, the composition Mo-13Si-12B, which has only 25% volume fraction of Mo(ss), has the least tensile strength and failure strain. Effect of grain size and volume fraction of T2 phase on tensile strength and failure strain is explained in further sections.

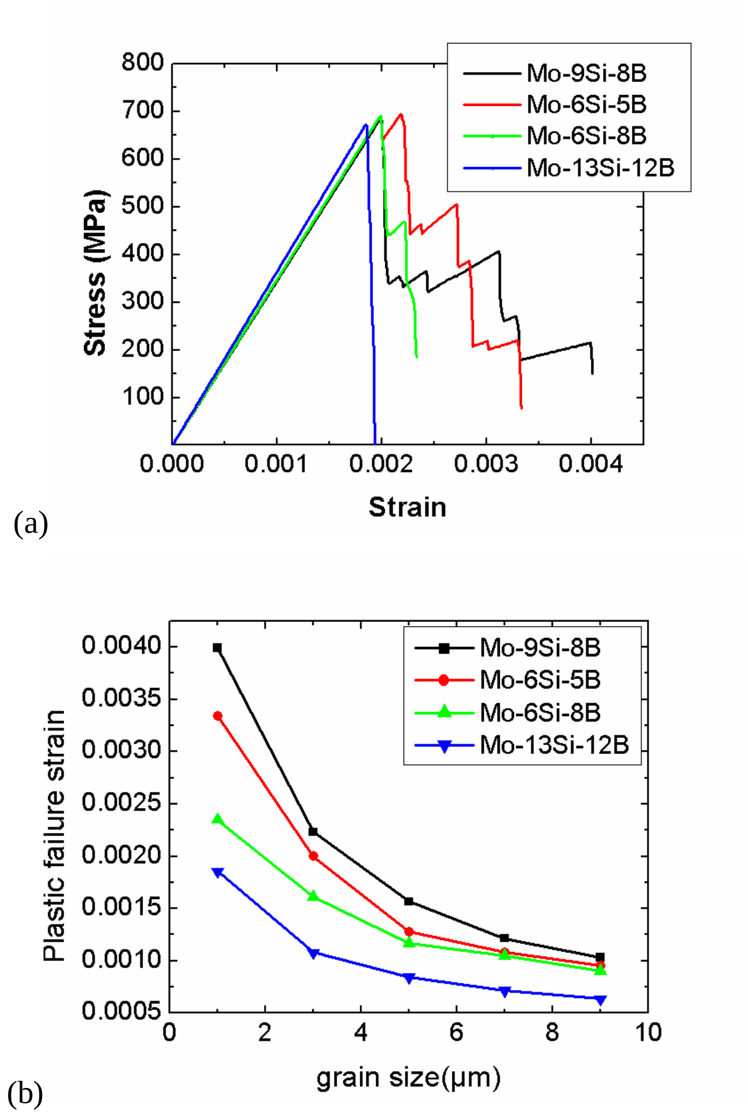

Fig. 6.3 (a) Tensile stress-strain curves for the simulated Voronoi structures of the alloy compositions for an average grain size of 1μm and (b) Curves showing the comparison of plastic failure strains of the simulated compositions for various grain sizes.

6.5.2 Influence of grain size on tensile strength

Three cases have been considered in this section to explain the influence of grain size on the tensile strength: 1) varying the grain size of all phases in the same way 2) Keeping the grain size of T2 phase constant and varying the grain sizes of Mo(ss) and T2 phases simultaneously and 3) keeping the grain sizes of two phases constant and changing the grain size of the remaining phase. The tensile strengths of various compositions, for each composition with different grain size considerations, obtained from simulations are shown in the table 6.2.

Grain size	**Tensile strength (MPa)**				
	Mo-6Si-5B	Mo-6Si-8B	Mo-9Si-8B	Mo-12Si-8.5B	Mo-13Si-12B
1µm	695	691	686	681	673
3µm	402	400	396	395	390
5µm	312	311	308	307	303
7µm	265	262	260	260	257
9µm	233	232	229	229	228

Table 6.2: Tensile strengths of various compositions at different grain sizes.

For case 1, the microstructure with fine grain size has a higher tensile strength than the one with coarser grain size and it’s gradually decreasing from finer grain to coarser grain microstructures as it shown in Fig 6.4 (a, b). Along with the strength, the initial and plastic failure strains of the material are increasing as the grain size of the microstructure is decreasing, as seen in the case of Mo-6Si-5B alloy composition. The same trend is observed for all other compositions when varying all the grain sizes in the same way.

In the second case, the Voronoi structure of composition 55-15-30 (Mo-9Si-8B) was taken exemplarily and the grain size of the T2 phase was kept constant while varying the grain sizes of both Mo(ss) and Mo_3Si phases simultaneously between 1µm and 9µm.

Grain sizes(µm)			Tensile strength (MPa)
Mo(ss)	Mo_3Si	T2	
1	**1**	**1**	**686**
3	**3**	**1**	**686**
5	**5**	**1**	**566**
7	**7**	**1**	**480**
9	**9**	**1**	**423**

Table 6.3: Influence of grain sizes of the other phases for 1µm constant grain size of T2 phase on tensile strength of 55-15-30 alloy composition.

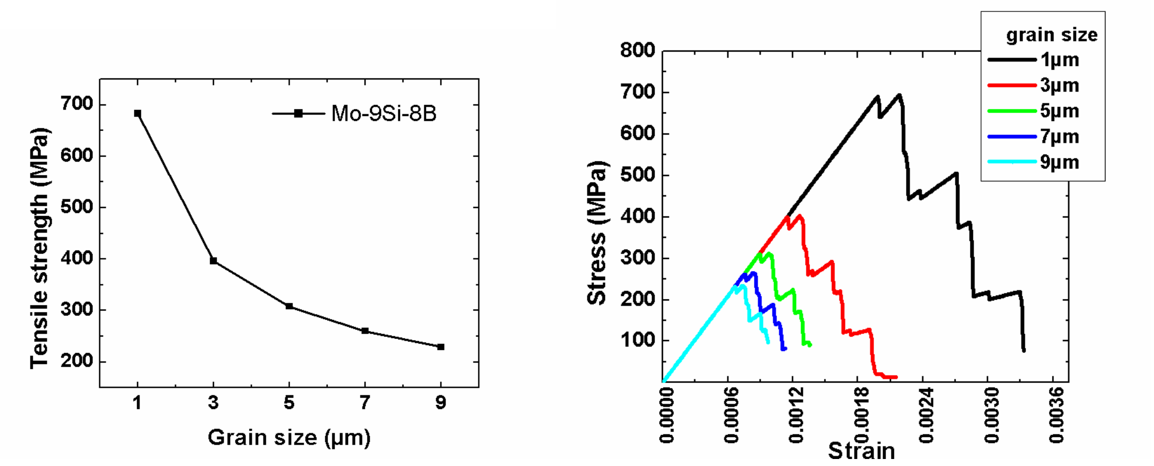

(a) (b)

Fig. 6.4 Simulation results of Voronoi structures showing (a) the variation of tensile strength of the Mo-9Si-8B alloy with grain size and (b) stress-strain curves of Mo-6Si-5B alloy composition at various grain sizes.

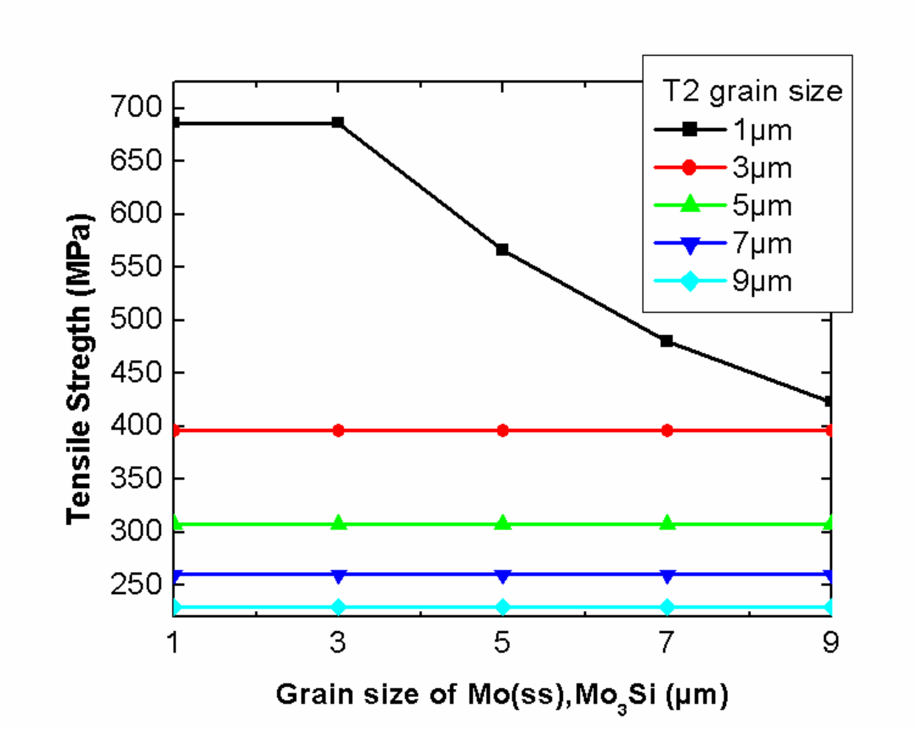

Fig. 6.5 Influence of grain sizes of the other phases for constant grain sizes, from 1μm to 9μm, of T2 phase on Tensile strength of 55-15-30 alloy composition.

For 1μm grain size of T2 phase, varying the grain size of Mo(ss) and Mo_3Si phase between 1μm and 3μm does not have any influence on tensile strength but varying them above 5µm has profound influence, (see fig.6.5). Influence of grain sizes of Mo(ss) and Mo_3Si phases at constant grain size of 1µm of T2 phase is presented in table 6.3. The tensile strength decreases as the grain sizes of the phases increase above 5µm at constant grain size of 1µm of T2 phase.

In the third case, the grain sizes of two phases were kept constant while varying the grain size of the remaining phase from 1µm to 9µm. The grain size of Mo(ss) phase does not a play decisive role as far as strength of the material is concerned. Its variation does not deteriorate mechanical properties of this 3-phase material, whereas Mo_3Si phase has a considerable influence provided the grain size of T2 phase is kept small compared to Mo_3Si. For example, (see Table 6.4), the microstructure with grain size of 1µm for all the phases has the same tensile strength as that with grain sizes 9µm-Mo(ss), 1µm-Mo_3Si and 1µm-T2. On the other hand, the microstructure with grain sizes 1µm-Mo(ss), 9µm-Mo_3Si and 1µm-T2 has a lower tensile strength compared to the microstructure with grain size of 1µm for all the phases, whereas the microstructure with grain sizes 1µm-Mo(ss), 3µm-Mo_3Si and 1µm-T2 has the same tensile strength as that of the microstructure with the grain size of 1µm for all the phases indicating that Mo_3Si phase has profound influence on the tensile strength for it’s larger grain sizes compared to that of T2 phase.

Grain sizes(µm)			Tensile strength (MPa)
Mo(ss)	Mo_3Si	T2	
1	**1**	**1**	**686**
9	1	1	686
7	1	1	686
5	1	1	686
3	1	1	686
1	**9**	1	**423**
1	1	**9**	**231**
1	**7**	1	**480**
1	1	**7**	**260**
1	**5**	1	**566**
1	1	**5**	**308**
1	**3**	1	**686**
1	1	**3**	**231**
1	**9**	**9**	**231**

Table 6.4: Influence of Mo(ss), Mo(ss) and T2 phases individually on the tensile strength of the 55-15-30 alloy composition.

6.6 Damage initiation and propagation

Crack was observed to initiate at the interfacial elements due to development of more stresses than applied stresses at the interfaces. Once the interfacial elements are failed the overall stress bearing capacity of the material decreases, and the average stress developed in the material decreases with the increase in the applied strain. It is known that T2 phase is more brittle than Mo(ss) and Mo_3Si phases present in the alloy, and Mo_3Si is more brittle than Mo(ss), and so as expected, the simulation results showed that damage always initiated at T2 phase if the grain size of all the phases are similar. In the exceptional cases where the grain size of Mo_3Si phase was more than 5 times than that of the T2 phase damage initiated in the Mo_3Si phase. Specifically, in the 55-15-30 alloy (in the order of Mo(ss)-Mo_3Si-T2), it was observed that for the microstructure with grain sizes 1µm-Mo(ss), 9µm-Mo_3Si, 1µm-T2, 1µm-Mo(ss), 7µm-Mo_3Si, 1µm-T2, and 1µm-Mo(ss), 5µm-Mo_3Si, 1µm-T2 damage initiated at Mo_3Si phase, whereas in all other cases damage initiated at T2 phase. The damage behaviour in the Voronoi model of alloy composition Mo-13Si-12B is shown in the figure 6.6, for the load applied in the horizontal direction. It can be observed that a crack initiates in the biggest grain of T2 phase and propagates back and forwards continuously. Here, the resistance against crack propagation was minor due to the absence of a sufficient volume percentage of Mo(ss) which is known to play an effective role in providing resistance to crack propagation by crack trapping at ambient temperatures and crack bridging mechanisms [11, 12] at high temperatures. The crack path is primarily confined to the Mo(ss) and Mo_3Si/T2 interface. Besides, the crack has a sufficient volume fraction of T2 phase to propagate through it avoiding the Mo(ss) phase.

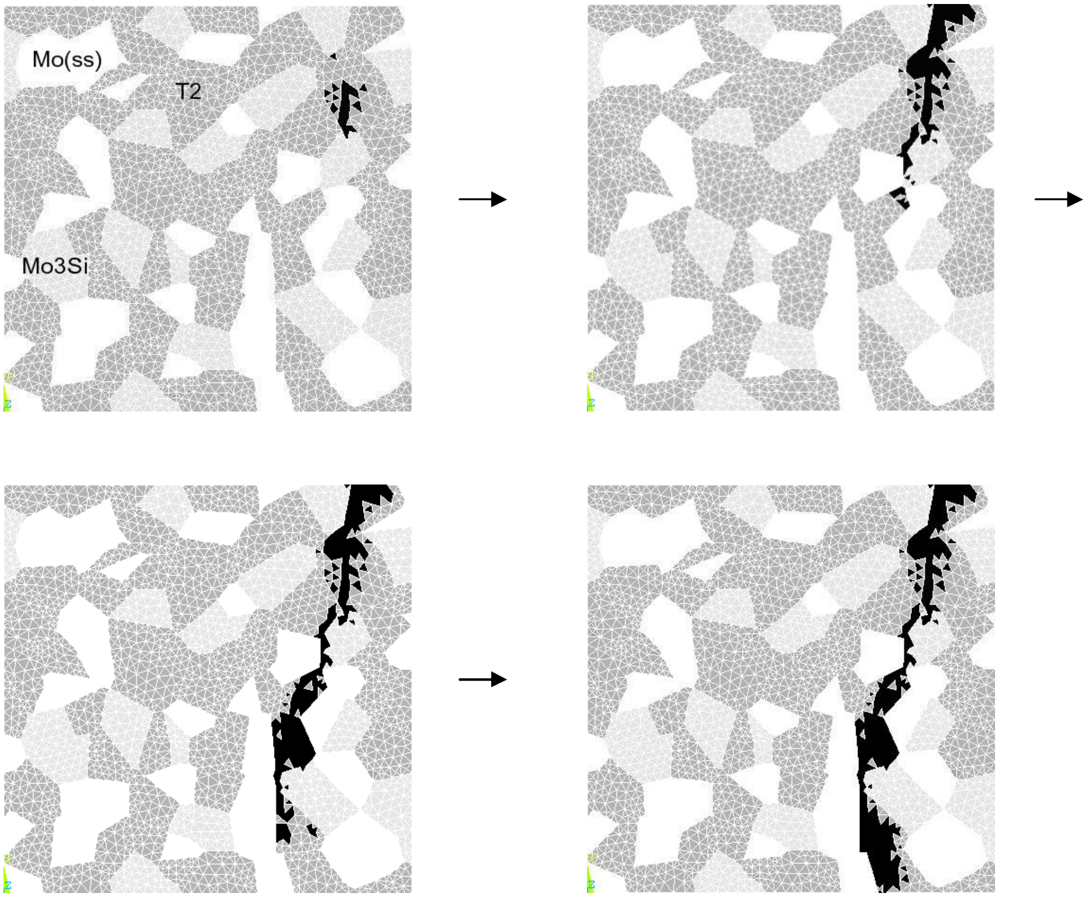

Fig. 6.6 Different stages from crack initiation to crack propagation in Voronoi model of Mo-13Si-12B alloy composition. (Tensile loading in horizontal direction)

Two-phase Voronoi structures of various compositions have been simulated under incremental tensile loading conditions. It was observed (see fig. 6.7) that for higher volume fractions of 78% and 89% of Mo(ss), micro cracking was developed in the T2 phase. The micro cracks could be developed due to toughening mechanism of Mo(ss) by crack bridging and there by providing some degree of crack growth resistance.

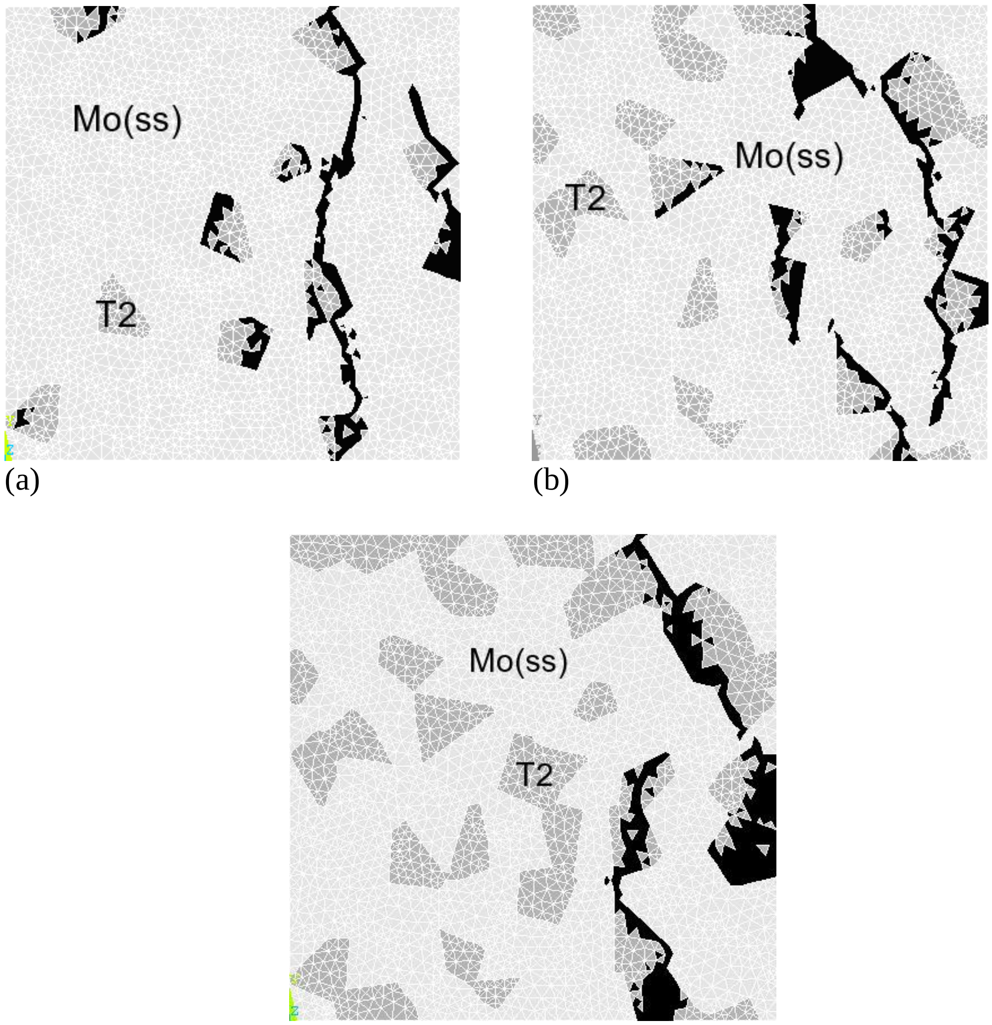

(a) (b)

(c)

Fig. 6.7 Crack paths under incremental tensile loading in the Voronoi structures of compositions (a) 89% Mo(ss)-11% T2 , (b) 78% Mo(ss)-22% T2 and (c) 67% Mo(ss)-33% T2.

6.7 Influence of volume fraction of the T2 phase on Tensile strength

As the T2 phase is more brittle than Mo(ss) and Mo_3Si, it is known that it has major influence on tensile strength and fracture toughness of the alloy. Therefore, seven different Voronoi structures of two-phase compositions, with Mo(ss) and T2 phases, have been modeled and finite element simulations were performed to observe the influence of volume fraction of T2 phase on tensile strength of the material.

The stress-strain curves for all the finite element simulated Voronoi models of two-phase compositions are compared in Fig. 6.8. Two significantly different behaviours may be noted here: while for volume fractions of Mo(ss) above 70%, the material showed considerable plastic strain, offering more resistance against crack growth, compositions with volume fractions of Mo(ss) of 56 %, 45 % and below showed essentially brittle behaviour which is also evident from the experimental results. Tensile strength was observed to be inversely proportional to volume fraction of T2 phase. Also, plastic failure strain decreased with an increase in grain size (see fig. 6.9).

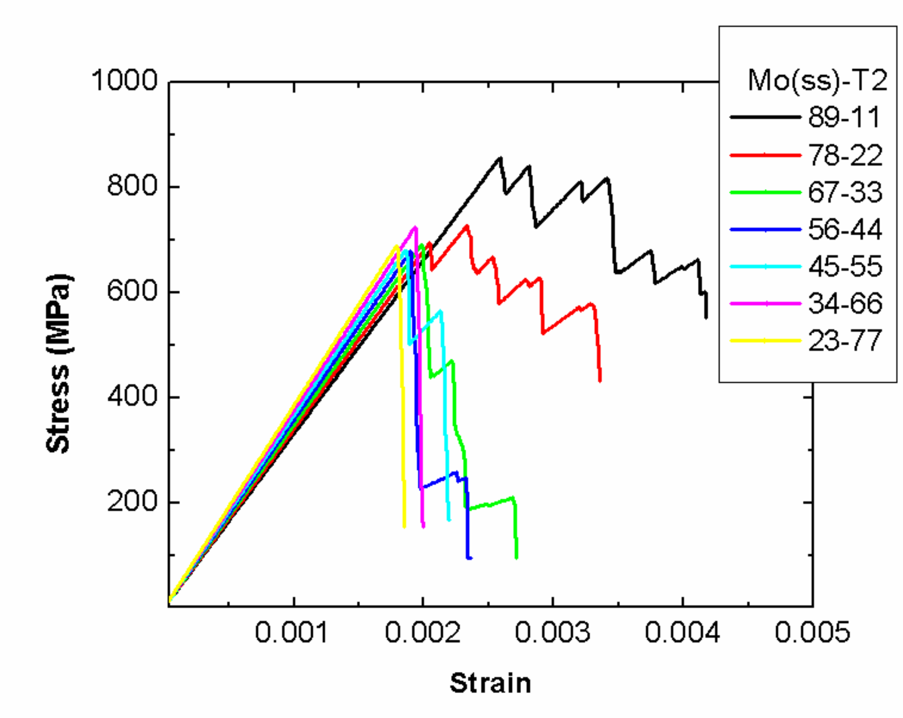

Fig. 6.8 Stress-strain curves of two-phase Mo(ss)-T2 composites with microstructure of 1μm grain size.

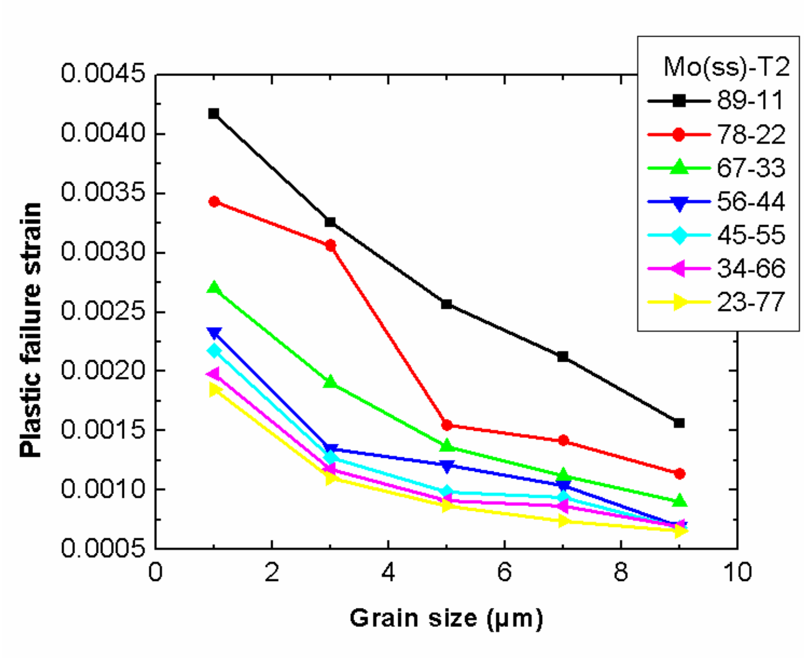

Fig. 6.9 Influence of volume fraction of Mo(ss)/T2 on plastic failure strain of the alloy for various grain sizes of the microstructure between 1µm and 9µm.

6.8 Comparison of simulation results with experiments

Stress - strain curve obtained from tensile testing of the alloy Mo-2.7Nb-8.9Si-7.7B at RT for both, the HIPed (see Fig. 5.1a(i) in chapter 5) and the annealed condition (see [38] for a microstructural image) are compared with those obtained from volume average stresses and strains of the FE simulated 55-15-30 alloy composition model. Two specimens of each microstructure were tensile tested at RT as explained in detail in the Chapter 3, section 3.1.2.1, and showed a substantial difference, namely, the annealed material with a microstructure coarser by a factor of 5 tends to fail at much lower stress [see Fig. 6.10]. Various Voronoi compositions of grain sizes between 1µm and 9µm were considered for simulation. FE simulation procedure is explained earlier in this Chapter, see section 6.3. It can be observed from Fig. 6.11, that the failure stress for the HIPed material lies in between the modelling curves for grain sizes of 1µm and 5µm, which is in good agreement with the microstructural result showing average grain sizes of around 1 µm for all three phases. Besides in [38], the annealed microstructures were determined to have average phase sizes between 4 and 7 µm and failure in this case occurred at a stress level of around 300 MPa which nicely coincides with the modelling of the 5 µm microstructure. Again this excellent agreement between experiment and model justifies the modelling approach chosen in this work.

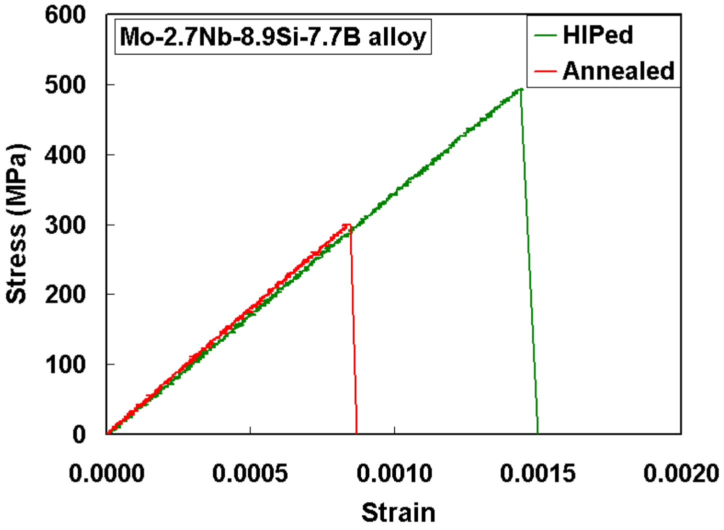

Fig. 6.10 Stress-strain curves for two of the tensile tested specimens of Mo-2.7Nb-8.9Si-7.7B alloy.

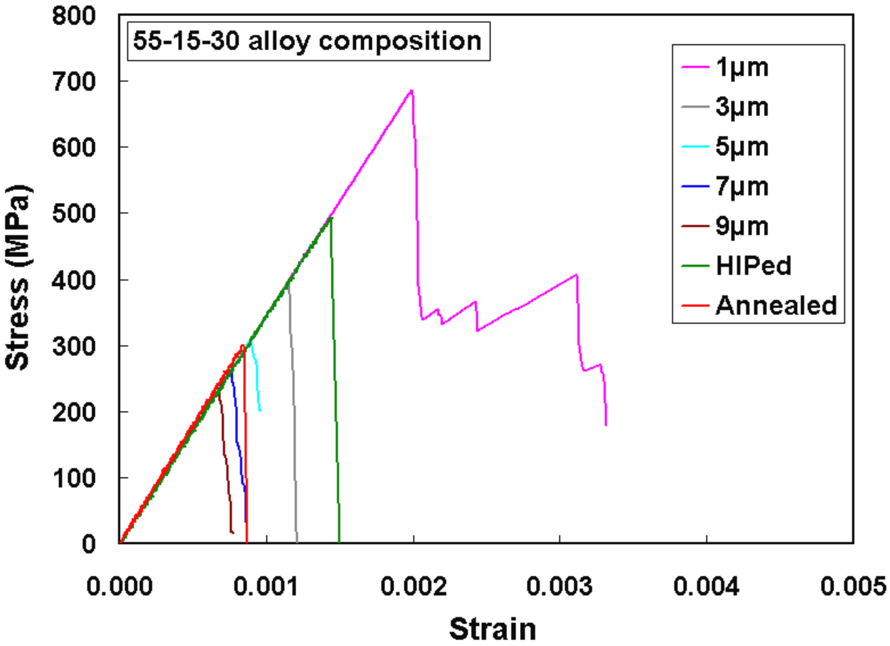

Fig. 6.11 Comparison of stress-strain curves obtained from the Experimental testing of the 55-15-30 alloy composition and FE Simulations of the same for various grain sizes of the microstructure between 1µm and 9µm.

Specimens	**Tensile strength (MPa)**						
	Experimental		FE Simulation				
HIPed 1	420	**458** (average)	1μm	3μm	5μm	7μm	9μm
HIPed 2	495		683	396	309	260	229
Annealed 1	299	**313** (average)					
Annealed 2	327						

Table 6.5: Comparison of tensile strengths obtained from experimental testing of Mo-2.7Nb-8.9Si-7.7B alloy and FE Simulation of the 55-15-30 alloy composition.

Chapter 7

Summary and Out look

The Mo-based silicide alloys earned significant attention in the recent years as the potential replacement for the currently used Ni-base single crystal superalloys for the application in aircraft/rotorcraft engines and in aero-derivative land-based gas turbines. To use them as such application materials, the knowledge about their temperature dependent elastic properties, strength and damage behaviour with their dependence on microstructure is essential. And to do so mechanically is extremely tedious and expensive. So in this thesis work the above mentioned properties were obtained through numerical approach and required experiments were conducted to justify the modelling approach.

The global hardness of Mo-Si-B alloy and the micro hardness values of its α-Mo matrix and intermetallics satisfy the linear rule of mixtures, from which the yielded volume fractions of the α-Mo matrix and intermetallic phases were in good agreement with those quantified by using IDL programming. The real and Voronoi microstructure simulations were implemented efficiently using Numerical Homogenization Technique to evaluate effective material properties of various compositions of Mo-Si-B. On the basis of the numerical investigations one can analyze the effect of microstructure on elastic properties, strength and damage behaviour of the Mo-base silicide alloy composites. Simple and efficient algorithms were developed in FORTRAN in order to perform a systematic numerical testing of microstructures of composites by applying incremental loading. Algorithms were developed to create Voronoi structures in MATHEMATICA, a high level programming language. An object oriented finite element program, PPM2OOF, was used to create finite element models.

The following points can be summarized from this thesis:

- The FEM results for the temperature dependent elastic properties of real microstructures and Voronoi structures are in good agreement with common analytical methods.

- There is no significant dependence of elastic material properties on grain size (this statement is valid for linear elastic case only), which was also evident from the experimental results. The annealed material of composition Mo2.7Nb8.9Si7.7B, with a coarser microstructure than that of the non-annealed one, of the same composition, by approximately one order of magnitude was observed to have almost identical elastic properties with a negligible difference of less than 2% between both microstructural states.

- A Voronoi structure may be taken as a good representative of a real microstructure of similar composition which is evident from the comparison of their calculated and measured elastic properties, respectively.

- The FEM results for the temperature dependent elastic properties of real microstructures are in very good agreement with the experimental results, with deviations of less than 2.6% for all parameters of interest. This proves that FEM approach chosen here is a reliable tool for modelling the elastic behaviour of the microstructure of a complex multi-phase material.

- The Voronoi composition of the alloy Mo-6Si-5B, which has 67% Mo(ss), has the highest tensile strength whereas Mo-9Si-8B (55% Mo(ss)) has the highest plastic failure strain compared to the other compositions, offering more resistance against failure of the material. The composition Mo-13Si-12B, which has 25% volume fraction of Mo(ss), has the least tensile strength and failure strain.

- Microstructures with finer grain sizes have generally a higher tensile strength than the one with coarser grain size and it’s gradually decreasing from finer grain to coarser grain microstructures.

- Plastic failure strains of the material are increasing as the grain size of the microstructure is decreasing.

- The grain size of Mo(ss) phase doesn’t play decisive role as far as strength of the material is concerned.

- Damage always initiated at T2 phase if the grain size of all the phases were similar. In the exceptional cases where grain size of Mo_3Si phase was more than 5 times to that of the grain size of T2 phase then damage initiated in the Mo_3Si phase.

- In the case of two phase compositions (Mo(ss)-T2), for volume fractions of Mo(ss) above 70%, the material showed considerable plastic strain, offering more resistance for the crack growth than the other compositions. And for compositions with more general volume fractions of Mo(ss) of 56 %, 45 % and below it showed more brittleness which is also evident from the experimental results.

- Plastic failure strain decreased with increase in grain size and was increasing with the increase in volume fraction of Mo(ss) in the composite.

- The composition 89%Mo(ss)-11%T2 has the highest tensile strength and plastic failure strains, where as 23%Mo(ss)-77%T2 has the least tensile strength and plastic failure strains for all the simulated grain sizes.

- The tensile strength of the alloy Mo-2.7Nb-8.9Si-7.7B obtained from experiments is comparable to that evaluated from FE simulation of 55-15-30 (in the order of volume fractions of Mo(ss)-Mo_3Si-T2) Voronoi composition of 3µm grain size and the experimental stress-strain curve was identical to those of the simulated compositions of various grain sizes, indicating that the modelling approach is successful.

Some directions for the extension of this work are given below:

Damage behaviour of the Mo-based silicide alloys at higher temperatures can be simulated using non-linear analysis introducing plasticity into the model i.e., assigning the Mo(ss) matrix and intermetallics the constitutive relations obtained from experimental observations at various temperatures and loading rates. The creep response of the two phase and three phase aggregates can also be simulated with this approach. It would be interesting to numerically study the effect of different kinds of arrangements of the phases and the grain shapes on the damage behaviour, failure stress and probability of the specimen failure of the composites using this Element Elimination Technique. This can be implemented with the Voronoi cell approach and by drawing artificial microstructures with varying fineness and nearest neighbourhood distance among the particles.

References

[1] Dimiduk, D. M., Perepezko, J. H., Mo-Si-B Alloys: Developing a revolutionary turbine-engine material, MRS Bulletin, 28 (9), 2003, 639-645.

[2] Bose, S., Engineering aspect of creep deformation of molybdenum disilicide, Materials Science and Engineering A, 155, 1992, 217–225.

[3] Yao, Z., Stiglich, J., Sudarshan, T. S., Molybdenum silicide based materials and their properties, Journal of Materials Engineering and Performance, 8, 1999, 291–304.

[4] Brady, M. P., Pint, B. A., Tortorelli, P. F., Wright I. G., and Hanrahan, Jr, R. J., Corrosion and Environmental Degradation II, In: Schütze, M., Editor, Wiley-VCH Verlag GmbH, Germany ,2000, Chapter 6, 297–305.

[5] Anton, D. L., Shah Mater, D. M., Research Society Symposium Proceedings, 213, 1991, 733–739.

[6] Meyer, M. K., Akinc, M., Isothermal oxidation behaviour of Mo-Si-B intermetallics at 1450°C, Journal of American Ceramic Society, 79, 1996, 2763–2766.

[7] Meyer, M. K., Akinc, M., Oxidation behaviour of boron-modified Mo5Si3 at 800°-1300°C, Journal of American Ceramic Society, 79**,** 1996, 938–944.

[8] Meyer, M. K., Thom, A. J., Akinc, M., Oxide scale formation and isothermal oxidation behaviour of Mo-Si-B intermetallics at 600-1000°C, Intermetallics, **7**, 1999, 153–162.

[9] Nunes, C. A., Sakidja, R., Perepezko, J. H., Phase stability in high temperature Mo-rich Mo-B-Si alloys, In: M.V. Nathal et al., Structural Intermetallics, 1997, TMS, Warrendale, PA, 1997, 831–839.

[10] Nowotny, H., Dimakopoulou, E., Kudielka, H., Untersuchungen in den Dreistoffsystemen: Molybdän-Silizium-Bor, Wolfram-Silizium-Bor und in dem System: VSi2-TaSi2, Mh. Chem., 88, 1957, 180-192.

[11] Choe, H., Schneibel, J. H., Ritchie, R. O., On the Fracture and Fatigue Properties of Mo-Mo_3Si-Mo_5SiB_2 Refractory Intermetallic Alloys at Ambient to Elevated Temperatures (25°C to 1300°C), Metallurgical and Materials Transactions, 34A, 2003, 225-239.

[12] Choe, H., D. Chen, D., Schneibel, J. H., Ritchie, R. O., Ambient to High Temperature Fracture Toughness and Fatigue-Crack Propagation Behaviour in a Mo-12Si-8.5B (at.%) Intermetallic, Intermetallics, 9, 2001, 319–329.

[13] Schneibel, J. H., Kramer, M. J., Ünal, Ö., Wright, R. N., Processing and mechanical properties of a molybdenum silicide with the composition Mo–12Si–8.5B (at.%), Intermetallics, 9, 2001, 25-31.

[14] Scruggs, D. M., Ductile Molybdenum composition containing a spinel dispersion, United States Patent 3,320,036, 1967.

[15] Burghard, Z., Zimmermann, A., Rödel, J., Aldinger, F., Lawn, B. R., Acta Materialia, 52, 2004, 293-297.

[16] http://periodic.lanl.gov/.

[17] http://www.webelements.com/webelements/elements/text/periodic-table/key.html.

[18] Kruzic, J. J., Schneibel, J. H., Ritchie, R.O., Fracture and fatigue resistance of Mo–Si–B alloys for ultrahigh-temperature structural applications, Scripta Materialia, 50, 2004, 459-464.

[19] Supatarawanich, V., Johnson, D. R., Liu, C. T., Effects of microstructure on the oxidation behaviour of multiphase Mo–Si–B alloys, Materials Science and Engineering. A, 344, 2003, 328-339.

[20] Sturm, D., Heilmaier, M., Schneibel, J. H., Jéhanno, P., Skrotzki, B., Saage, H., The influence of silicon on the strength and fracture toughness of molybdenum, Materials Scieince and Engineering A, 463, 2007, 107-114.

[21] Stephens, J. R., Klopp, W. D., Transactions of the Society of Mining Engineers of AIME, 242, 1968, 1837-1843.

[22] www.specialtymetals.com.

[23] Vasudévan, A. K., Petrovic, J., A comparative overview of molybdenum silicide composites, Materials Scieince and Engineering A, 155, 1992, 1-17.

[24] Meyer, M. K., Kramer, M. J., Akinc, M., Compressive creep behaviour of Mo5Si3 with the addition of boron, Intermetallics, 4, 1996, 273-281.

[25] Akinc, M., Meyer, M. K., Kramer, M. J., Thom, A. J., Huebsch, J. J., Cook, B., Boron-doped molybdenum silicides for structural applications, Materials Scieince and Engineering A, 261, 1999, 16-23.

[26] Meyer, M. K., Thom, A. J., Akinc, M., Oxide scale formation and isothermal oxidation behaviour of Mo-Si-B intermetallics at 600-1000°C, Intermetallics, 7, 1999, 153-162.

[27] Berczik, M., Method for enhancing the oxidation resistance of a molybdenum alloy, and a method of making a molybdenum alloy, United States Patent 5,595,616, 1997.

[28] Berczik, D. M., Oxidation Resistant Molybdenum Alloys, United States Patent 5,693,156, 1997.

[29] Jéhanno, P., Heilmaier, M., Saage, H., Heyse, H., Böning, H., Kestler, H., Schneibel, J. H., Scripta Materialia, 55, 2006, 525-528.

[30] Gunter, I. M., Schneibel, J. H., Kruzic, J. J., Materials Science and Engineering A, 458, 2007, 275–280.

[31] Schneibel, J. H., High temperature strength of Mo–Mo_3Si–Mo_5SiB_2 molybdenum silicides, Intermetallics, 11, 2003, 625-632.

[32] Schneibel, J. H., Ritchie, R. O., Kruzic, J. J., Tortorelli, P. F., Optimizaton of Mo-Si-B Intermetallic Alloys, Metallurgical and Materials Transactions, 36A, 2005, 525-531.

[33] Leichtfried, G., Schneibel, J. H., Heilmaier, M., Ductility and Impact Resistance of Powder-Metallurgical Molybdenum-Rhenium Alloys, Metallurgical and Materials Transactions, 37A, 2006, 2955-2961.

[34] Schneibel, J. H., Kramer, M. J., Easton, D. S., A Mo–Si–B intermetallic alloy with a continuous α-Mo matrix, Scripta Materialia, 46, 2002, 217-221.

[35] Schneibel, J. H., Liu, C. T., Easton, D. S., Carmichael, C. A., Materials Science and Engineering A, 261, 1999, 78-83.

[36] Lins, W., Kaindl, G., Peterlik, H., Kromp, K., A novel resonant beam technique to determine the elastic moduli in dependence on orientation and temperature up to 2000°C, Review of Scientific Instruments, 70(7), 1999, 3052-3058.

[37] European standard EN 843-2 (2005-01).

[38] Jéhanno, P., Heilmaier, M., Saage, H., Böning, M., Kestler, H., Freudenberger, J., Drawin, S., Assessment of the high temperature deformation behaviour of molybdenum silicide alloys, Materials Science and Engineering A, 463, 2007, 216-223.

[39] Richard, H. A., Interpolationsformeln für Spannungsintensitätsfaktoren, VDI-Z, 1979, Nr.22, 1138-1143.

[40] Brown, W. F. and Srawley, J. E., Plane strain crack toughness testing of high strength metallic materials, ASTM STP 410, 1966, 46-51.

[41] http://www.ittvis.com/idl/.

[42] Voigt, W., Über die Beziehung zwischen den beiden elastizitätskonstanten isotroper Körper, Annalen der Physik und Chemie, 38, 1889, 573-587.

[43] Reuss, A., Berechung der Fliessgrenze von Mischkristallen auf Grund der Plastizitätsbedingung für Einkristalle, Zeitschrift für Angewandte Mathematik und Mechanik, 9, 1992, 49-58.

[44] Hashin, Z., The elastic moduli of heterogeneous materials, Journal of Applied Mechanics, 29, 1962, 143-150.

[45] Hashin, Z., Shtrikman, S., A variational approach to the theory of the elastic behaviour of multiphase materials, Journal of the Mechanics and Physics of Solids, 211, 1963, 127-140.

[46] Halpin, J. C., Kardos, J. L., The Halpin-Tsai equations: a review. Polymer Engineering and science, 16(5), 1976, 344-352.

[47] Hill, R., A self-consistent mechanics of composite materials, Journal of the Mechanics and Physics of Solids, 13, 1965, 213-222.

[48] Kröner, E., Berechung der elastischen Konstanten des vielkristalls aus den Konstanten des Einkristalls, Zeitschrift für Physik, 151, 1958, 504-518.

[49] Hashin, Z., Rosen, B. W., The elastic moduli of fiber-reinforced materials, Journal of Applied Mechanics, 31, 1964, 223-232.

[50] Hershey, A. V., The elasticity of an isotropic aggregate of anisotropic cubic crystals, Journal of the Mechanics and Physics of Solids, 11, 1954, 127.

[51] Wolfram, S., http://www.wolfram.com.

[52] Langer, S., Fuller, E., OOF, NIST, Gaithersburg, MD, 1997.

[53] Jean-Marie Berthlot, Composite materials – mechanical behaviour and structural analysis, Springer – Verlag, New York, 1999.

[54] Berger, H., Kari, S., Gabbert, U., Rodriguez-Ramos, R., Guinovartdiaz, R., Otero, J. A., Bravo-Castillero, J., An analytical and numerical approach for calculating effective material coefficients of piezoelectric fiber composites, International Journal of Solids and Structures, 42, 2005, 5692-5714.

[55] Smith, S. C., Experimental values for the elastic constants of a particulate filled glassy polymer, Journal of Research of the National Bureau of Standards section A-Physics and Chemistry, 80A, 1976, 45-49.

[56] Ihara, K., Ito, K., Tanaka, K., Yamaguchi, M., Mechanical properties of Mo5SiB2 single crystals, Materials Science and Engineering A, 329, 2002, 222-227.

[57] Ito, K., Ihara, K., Tanaka, K., Fujikura, M., Yamaguchi, M., Physical and mechanical properties of single crystals of the T2 phase in the Mo-Si-B system, Intermetallics, 9, 2001, 591-602.

[58] Fu, C. L., private communications.

[59] Meyer, M. K, Kramer, M. J, Akinc, M., Compressive creep behaviour of Mo_5Si_3 with the addition of boron, Intermetallics, 4, 1996, 273-281.

[60] Meyer, M. K., Akinc, M., Isothermal Oxidation Behaviour of Mo–Si–B. Intermetallics at 1450°C, Journal of the Americal Ceramic Society, 79, 1996, 2763-2766.

[61] Meyer, M. K., Thom, A. J., Akinc, M., Oxide scale formation and isothermal oxidation behaviour of Mo–Si–B intermetallics at 600–1000°C, Intermetallics, 7, 1999, 153-162.

[62] Berczik, D. M., Method for enhancing the oxidation resistance of a molybdenum alloy, and a method of making a molybdenum alloy. United States Patent 5,595,616, 1997.

[63] Berczik, D. M., Oxidation resistant molybdenum alloys. United States Patent 5,693,156, 1997.

[64] Supatarawanich, V., Johnson, D. R., Dayananda, M. A., Liu, C. T., Processing and Properties of Multiphase Mo-Si-B Alloys, Materials Science Forum, 426-432, 2003, 4301-4306.

[65] Mishnaevsky Jr., L., Dong, M., Hoenle, S., Schmauder, S., Computational Mesomechanics of Particle-Reinforced Composites, Computational Materials Science, 16(1–4), 1999, 133–143.

[66] Mishnaevsky Jr., L., Schmauder, S., Continuum Mesomechanical Finite Element Modelling in Materials Development: a State-of-the-Art Review, Applied Mechanics Reviews, 54(1), 2001, 49–69.

[67] Wulf, J., Neue finite-elemente-methode zur simulation des duktilbruchs in Al/SiC. Dissertation, MPI für Metallforschung, Stuttgart, 1995.

[68] Tvergaard, V., Studies of void growth in a thin ductile layer between ceramics, Computational Mechanics, 20, 1997, 184-191.

[69] Broeckmann, C., Bruch karbidreicher Stähle – Experiment und FEM-Simulation unter Berücksichtigung des Gefüges, Dissertation, Ruhr- Universitaet Bochum, 1994.

[70] Mishnaevsky Jr., L., Lippmann, N., Schmauder, S., Computational modelling of crack propagation in real microstructures of steels and virtual testing of artificially designed materials, International Journal of Fracture, 120, 2003, 581–600.

[71] Rosales, I., Schneibel, J. H., Stoichiometry and mechanical properties of Mo_3Si, Intermetallics, 8, 2000, 885-889.

[72] http://rsb.info.nih.gov/ij/.

[73] http://www.ultmat.onera.fr/index.html.

[74] http://www.gordonengland.co.uk/hardness/hvconv.htm